

High-Time-Cadence Spectroscopy and Photometry of Stellar Flares on M-dwarf YZ Canis Minoris with Seimei Telescope and TESS. I. Discovery of Rapid and Short-Duration Prominence Eruptions

YUTO KAJIKIYA,¹ KOSUKE NAMEKATA ^{2,3,4} YUTA NOTSU ^{5,6} HIROYUKI MAEHARA ⁷ BUNEI SATO ¹ AND
DAISAKU NOGAMI ⁸

¹*Department of Earth and Planetary Sciences, Tokyo Institute of Technology
2-12-1 Ookayama, Meguro-ku, Tokyo 152-8551, Japan*

²*The Hakubi Center for Advanced Research, Kyoto University, Kyoto 606-8302, Japan*

³*Department of Physics, Kyoto University, Kitashirakawa-Oiwake-cho, Sakyo-ku, Kyoto, 606-8502, Japan*

⁴*Division of Science, National Astronomical Observatory of Japan, NINS, Osawa, Mitaka, Tokyo, 181-8588, Japan*

⁵*Laboratory for Atmospheric and Space Physics, University of Colorado Boulder 3665 Discovery Dr, Boulder, CO 80303, USA*

⁶*National Solar Observatory, 3665 Discovery Drive, Boulder, CO 80303, USA*

⁷*Okayama Branch Office, National Astronomical Observatory of Japan
3037-5 Honjo, Kamogata-cho, Asakuchi, Okayama 719-0232, Japan*

⁸*Department of Astronomy, Kyoto University, Kitashirakawa Oiwake-cho, Sakyo-ku, Kyoto 606-8502, Japan*

ABSTRACT

M-dwarfs show frequent flares and associated coronal mass ejections (CMEs) may significantly impact close-in habitable planets. M-dwarf flares sometimes show red/blue asymmetries in the H α line profile, suggesting prominence eruptions as an early stage of CMEs. However, their high-time-cadence observations are limited. We conducted spectroscopic monitoring observations of the active M-dwarf YZ Canis Minoris with ~ 1 minute time cadence using the Seimei telescope, simultaneously with the optical photometric observations by Transiting Exoplanet Survey Satellite. We detected 27 H α flares with H α energies ranging from 1.7×10^{29} to 3.8×10^{32} erg and durations from 8 to 319 minutes. Among them, we identified 3 blue asymmetry and 5 red asymmetry events based on criteria using the Bayesian Information Criterion. The maximum velocity of the blue- and red-shifted components ranges from 250 to 450 km s⁻¹ and 190 to 400 km s⁻¹, respectively. The duration and time evolution show variety, and in particular, we discovered rapid, short-duration blue/red asymmetry events with the duration of 6–8 minutes. Among the 8 blue/red asymmetry events, two blue and one red asymmetry events are interpreted as prominence eruptions because of their fast velocity and time evolution. Based on this interpretation, the lower limit of occurrence frequency of prominence eruptions can be estimated to be ~ 1.1 events per day. Our discovery of short-duration events suggests that previous studies with low time cadence may have missed these events, potentially leading to an underestimation of the occurrence frequency of prominence eruptions/CMEs.

Keywords: Stellar flares (1603); Stellar coronal mass ejections (1881); Optical flares (1166); M dwarf stars (982); Flare stars (540)

1. INTRODUCTION

Solar and stellar flares are explosive phenomena that occur suddenly in the corona of the Sun and stars (e.g., Kowalski 2024). They are observed as an increase in electromagnetic radiation, ranging from X-rays to radio waves. These flares are believed to be caused by the conversion of magnetic energy into kinetic and thermal energy through magnetic reconnection (Shibata & Magara 2011). Some of the energy released in the corona is transported to the chromosphere and photosphere via heat conduction and high-energy particles. This leads to chromospheric evaporation, chromospheric condensation, and radiation from the corona, transition region, chromosphere, and photosphere (e.g., Fisher et al. 1985; Allred et al. 2006). Part of the magnetic energy is released for plasma ejections known as prominence/filament eruptions. On the Sun, they often develop into coronal mass ejections (CMEs), which can significantly impact Earth’s environment (e.g., Bisi et al. 2010; Gopalswamy 2016).

In recent years, M-dwarfs are considered as prime targets for the search for habitable planets (Nutzman & Charbonneau 2008; Gilbert et al. 2020) and have been observed to show very high flare activity. Superflares with more than ten times the energy of the largest solar flares are observed (Namizaki et al. 2023). If CMEs associated with these superflares can eject from the stellar surface, the impact on surrounding close-in planets would be significant. Large CMEs could cause atmospheric erosion if they collide with a close-in planet (Lammer et al. 2007). Additionally, high-energy particles accelerated by fast shocks produced during CMEs could promote chemical reactions in planetary atmosphere (Airapetian et al. 2016). This could potentially lead to the origin of life-essential molecules such as amino acids (Kobayashi et al. 2023). Since M-dwarfs have habitable zones closer to the star compared to G-dwarfs and K-dwarfs, such impacts on close-in habitable planets can be greater (Lingam et al. 2018). Therefore, understanding the frequency and energy of prominence/filament eruptions, and eventually CMEs, in active M-dwarfs is crucial for evaluation of habitable condition of exoplanets.

Over the past several decades, optical spectroscopic observations have revealed that chromospheric line profiles often show blue asymmetries during flares on M-dwarfs, suggesting possible prominence/filament eruptions (e.g., Houdebine et al. 1990; Vida et al. 2016, 2019; Maehara et al. 2021; Notsu et al. 2024; Inoue et al. 2024). Vida et al. (2016) reported a blueshifted component with a maximum radial velocity of 675 km s^{-1} during an $H\alpha$ flare on the M4 dwarf V374 Peg. Additionally, Vida et al. (2016) observed an $H\alpha$ flare where a red asymmetry followed the blue asymmetry in the $H\alpha$ line, suggesting that some of the ejected low-temperature plasma returns to the stellar surface. Honda et al. (2018) reported a long-duration blue asymmetry lasting about 2 hours at a velocity of approximately 100 km s^{-1} during an $H\alpha$ flare on the M4.5 dwarf EV Lac. Maehara et al. (2021) reported a blue asymmetry lasting about 1 hour without significant white-light brightening (a possible non-white-light flare) during an $H\alpha$ flare on the M4.5 dwarf YZ CMi. Furthermore, Inoue et al. (2024) reported a blue asymmetry appearing about 1 hour after the peak of an $H\alpha$ flare on the M4.5 dwarf EV Lac. Notsu et al. (2024) reported 7 blue asymmetries among 41 $H\alpha$ flares in the M-dwarfs YZ CMi, EV Lac, and AD Leo, with durations ranging from approximately 20 minutes to 150 minutes and velocities ranging from about 73 km s^{-1} to 122 km s^{-1} . It has been discussed that they can be interpreted as prominence/filament eruptions based on the velocity and mass. However, the time cadence ($>5 \text{ min}$) of the previous observations is not necessarily high enough to capture and trace the rapid velocity changes of prominence eruptions on M-dwarfs with strong surface gravity. Actually, some solar prominence/filament eruptions change their velocities in less than 5 minutes (Otsu et al. 2022). Higher-time-cadence ($\sim 1 \text{ min}$) is essentially required not to miss even such short-duration/fast phenomena especially for M-dwarfs.

Meanwhile, the nature and origin of the $H\alpha$ blue asymmetries during M-dwarf flares are still under debate, and simultaneous observations with multiple wavelength ranges and different methods (e.g., photometry) are useful for this purpose. For example, the blue asymmetries could also be explained by the upward flow of low-temperature plasma associated with chromospheric evaporation, as observed in the early stage of solar flares (Tei et al. 2018; Canfield et al. 1990). However, white-light flares represent the emission only from flare ribbons originated from chromospheric evaporation/condensation during impulsive phase (Watanabe et al. 2013; Namekata et al. 2017), thus it is crucial to compare the emission energy and temporal variation of white-light emission with those of $H\alpha$ blue asymmetries. One-month continuous photometric observations by the Transiting Exoplanet Survey Satellite (TESS, Ricker et al. 2015) have enabled simultaneous photometric and spectroscopic observations, providing a good opportunity to investigate statistical relationships between blue asymmetries and white-light flares, rotational phase which reflects starspots distribution (Ikuta et al. 2023). From these statistical investigations, we can explore the typical properties of blue asymmetries on M-dwarfs, including the location of occurrence. Previous studies with such simultaneous observations using white-light photometry and $H\alpha$ line spectroscopy (Maehara et al. 2021; Namizaki et al. 2023; Notsu et al. 2024) reported only three blue asymmetries during the non-white-light flares or a partial white-light flare (occurring not concurrently with the white-light flare, but shortly after its decay) observed by TESS. The number of such observations is still small, and there are no systematic studies using monitoring observations by TESS.

In this study, we conducted high-time-resolution (approximately 1 minute) $H\alpha$ line spectroscopic observations of the active M-dwarf YZ CMi using the Seimei telescope (Kurita et al. 2020). Simultaneously, high-precision optical photometric observations were conducted by TESS. We performed this simultaneous campaign observation for 12 nights. This significantly increases the sample size of observations of $H\alpha$ red/blue asymmetries for white-light/non-white-light flares, which is expected to be helpful to identify the origin of blue asymmetries. For this statistical sample, we incorporated a new criteria to identify the asymmetric or symmetric profiles by using the Bayesian Information Criterion (BIC; Section 3.3). The data and observations are described in Section 2. The analysis methods are explained

in Section 3. The analysis results are presented in Section 4. A detailed discussion of the H α blue asymmetries is in Section 5. The summary and conclusions are provided in Section 6.

2. OBSERVATION AND DATA

2.1. Target Star: YZ CMi

YZ CMi is an M4.5-type dwarf known as a flare star, with a thick convective zone and rapid rotation. Zeeman-Doppler Imaging by Morin et al. (2008); Lang et al. (2014) reported YZ CMi had a large-scale dipole magnetic field in 2007 and 2008. Table 1 lists the stellar parameters of YZ CMi. Since the first observation of flares on YZ CMi by van Maanen et al. (1945), numerous flares across a wide range of wavelengths from X-rays to radio have been observed. Furthermore, superflares with the energies of $>10^{33}$ erg, which are more than 10 times larger than the largest solar flares ($\sim 10^{32}$ erg), have also been detected (Maehara et al. 2021), indicating an exceptionally high level of flare activity.

Table 1. Stellar Parameters

Parameter	Value
Effective Temperature T_{eff} (K)	$3280 \pm 73^{\dagger}$
Rotation Period P_{rot} (day)	$2.774 \pm 0.0014^{\ddagger}$
Stellar Radius R_{star} (R_{\odot})	$0.37^{+0.03}_{-0.06}^{\S}$
Stellar Mass M_{star} (M_{\odot})	$0.37 \pm 0.01^*$
Distance d (pc)	$5.99 \pm 0.0012^{**}$
Radial Velocity v_{RV} (km s^{-1})	$26.66 \pm 0.0033^{\dagger\dagger}$

[†] Gaidos & Mann (2014).

[‡] Maehara et al. (2021).

[§] Baroch et al. (2020).

^{*} Cifuentes et al. (2020).

^{**} Gaia Collaboration et al. (2023).

^{††} Fouqué et al. (2018).

2.2. TESS

TESS is a space telescope designed for the search of exoplanets using the transit method. It divides the entire sky into sectors of 24° by 96° , conducting continuous photometric observations for approximately 27.4 days per sector. TESS covers wavelength range from 6000 to 10000 Å. YZ CMi was observed by TESS during observations of Sector 34 from January 14 to February 8, 2021 (Barycentric Julian Date (BJD): 2459229.09 – 2459245.07). In this study, we used the Pre-search Data Conditioned Simple Aperture Photometry (PDC-SAP) light curve obtained from the Mikulski Archive for Space Telescopes (MAST) portal¹. Figure 1 (a) shows the light curve of YZ CMi observed by TESS at a 20-sec cadence.

2.3. 3.8m Seimei Telescope

The spectroscopic observations were conducted with the Seimei telescope at the same time as the photometric observations at TESS. The Seimei telescope, located at the Okayama Observatory, is a 3.8-meter telescope (Kurita et al. 2020) equipped with the low-dispersion spectrograph KOOLS-IFU (Kyoto Okayama Optical Low-dispersion Spectrograph with an optical-fiber integral field unit; Matsubayashi et al. 2019). The data of YZ CMi in this study were obtained from January 18 to February 4, 2021, using the KOOLS-IFU spectrograph and the VPH683 grism (wavelength range 5800–8000Å, spectral resolution $\lambda/\Delta\lambda \sim 2000$). Observations were conducted over 13 clear nights, with 67 hours of actual observing time. The observed wavelength range included the H α line (6562.8Å). The velocity resolution around the H α line was approximately 150 km/s, with a sampling of approximately 50 km/s per pixel. This line is a crucial chromospheric line indicating flare activity. The exposure time was set to 60 seconds and the readout time is ~ 17 seconds, resulting in the time cadence of ~ 77 seconds. This high temporal resolution spectroscopy enables

¹ <https://mast.stsci.edu/>

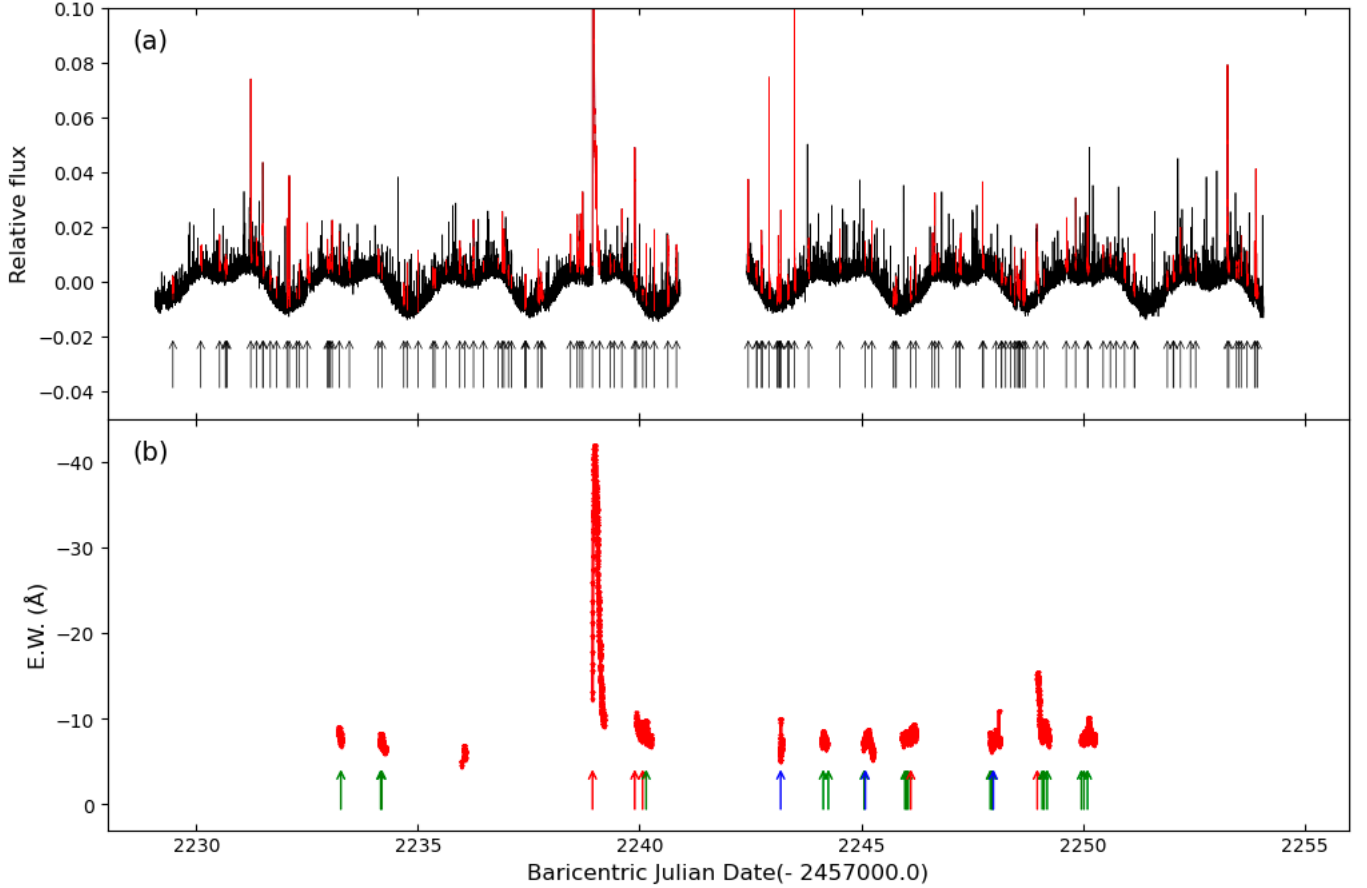


Figure 1. (a) Light curve observed by TESS at a 20-second cadence. The horizontal axis represents BJD, while the vertical axis represents the relative flux normalized to the average ($\delta F/F_{\text{av}}$). The upward arrows in the figure indicate the start times of the detected white-light flares, and the red solid lines show their durations. (b) Light curve of the H α line observed by the Seimei Telescope. The horizontal axis represents BJD, while the vertical axis represents the equivalent width of the H α line. The upward arrows in the figure indicate the start times of the detected H α flares. Red arrows point to flares showing red asymmetry, blue arrows to flares showing blue asymmetry, and green arrows to flares showing no asymmetry.

detailed investigations of spectral changes in the H α line during stellar flares. Initial data processing followed the methods outlined by Namekata et al. (2020, 2022); Namizaki et al. (2023), using packages from IRAF (Tody 1986) and PyRAF (Science Software Branch at STScI 2012). The process includes the bias subtraction, gain correction, and wavelength calibration. We did not use the fibers which include the significant cosmic-ray contamination around the H α line. Additionally, each spectrum was corrected for the radial velocity v_{RV} of YZ CMi (26.66 km s $^{-1}$; Fouqué et al. 2018). The spectra were normalized based on the continuum near the H α line, and the intensity of the H α line was integrated over the range of 6562.8 ± 15 Å, to calculate the equivalent width of the H α line. Figure 1 (b) shows the light curve of the H α line equivalent width observed by the Seimei Telescope.

3. ANALYSIS

3.1. TESS White-Light Flare Detection

We detected white-light flares from the TESS light curve using the method similar to that of Maehara et al. (2021). We analyzed the PDC-SAP light curve of YZ CMi from TESS Sector 34 with the 20s cadence. Before the flare detection process, we first removed non-flare signals such as long-term trends and brightness variations due to rotation from the light curve. Initially, we fitted the long-term variations in the light curve with a 5th-degree spline function and subtracted the result from the original light curve to eliminate non-flare signals. In the processed light curve, any increase in brightness exceeding 3σ (σ : the average photon noise of the light curve) for three consecutive data points was selected as a flare (cf., Chang et al. 2015). The bolometric energy of the detected white-light flares was

calculated assuming a blackbody radiation of 10000 K and the TESS response function, following the method described by Shibayama et al. (2013). The duration of the detected flares was calculated from the point where the brightness increase first exceeded 1σ until it decreased below 1σ for two consecutive points.

3.2. $H\alpha$ Flare Detection

The detection of $H\alpha$ flares was conducted using the light curve of the $H\alpha$ line at the same time as the photometric observations at TESS. For the detection method, an increase in the absolute value of the equivalent width of the $H\alpha$ line by more than 3σ (σ : standard deviation of the equivalent width values in the quiescent state) from the quiescent state spectra², persisting for three consecutive data points, was identified as a flare. The duration over which the absolute value of the equivalent width remained above 1σ from the quiescent state spectra was considered as part of the same flare. This method has the uncertainty of potentially counting multiple flares as a single flare or counting a single flare as multiple flares.

Next, we calculate the energy of detected $H\alpha$ flares, following the approach by Namizaki et al. (2023). First, the $H\alpha$ flux, $F_{H\alpha}$, was calculated by multiplying the $H\alpha$ equivalent width by the continuum flux near the $H\alpha$ line. The quiescent state continuum flux was derived from values obtained from quiescent state spectra that had been calibrated for flux according to Kowalski et al. (2013). Using $F_{H\alpha}$ and the distance between YZ CMi and Earth ($d = 5.99$ pc; Gaia Collaboration et al. 2023), the $H\alpha$ luminosity was then calculated based on the equation:

$$L_{H\alpha} = 4\pi d^2 F_{H\alpha} \quad (1)$$

Following Notsu et al. (2024), we used TESS's relative flux $\delta F/F_{av}$ to account for the increase in the continuum flux near the $H\alpha$ line during the flare duration. We note that the wavelengths of the TESS band and the $H\alpha$ line are different. Therefore, the changes in the continuum flux near the $H\alpha$ line may be slightly different from the changes in the TESS band flux. Subsequently, the differential luminosity, $L_{H\alpha,flare}$ ($= L_{H\alpha} - L_{H\alpha,quie}$, where $L_{H\alpha,quie}$ is the quiescent state luminosity), was integrated over the duration of the $H\alpha$ flare to calculate the energy of the $H\alpha$ flare according to the equation:

$$E_{H\alpha} = \int L_{H\alpha,flare}(t) dt \quad (2)$$

The duration of the detected $H\alpha$ flares was determined from the point where the equivalent width of the $H\alpha$ line increased more than 1σ from the quiescent state to the point where it decreased below 1σ .

3.3. Detection of $H\alpha$ Line Profile Asymmetry

We introduce the method for determining the asymmetry of the $H\alpha$ line spectrum. First, to extract the flare components, the normalized spectrum in the quiescent state was subtracted from the normalized spectrum during the flare duration (see Figure 2 (a)). Next, the differential spectrum created in this section was fitted with two models suitable for symmetric and asymmetric spectra, respectively: a Voigt function (magenta solid line in Figure 2 (b)) for symmetric spectra and a combined model (a sum of a Voigt function and a Gaussian function, blue dash-dotted line in Figure 2 (b)) for asymmetric spectra. In this fitting, the center of the Voigt function was fixed within the range of 6562 Å to 6564 Å for both models. This is done to prevent the influence of line profile asymmetry due to the shift between the center of the $H\alpha$ line (6562.8 Å) and the peak of the observed data caused by insufficient wavelength resolution. Additionally, the width σ of the Gaussian function was set to be at least half the wavelength resolution during the fitting. Subsequently, BIC for each model was calculated, and the difference in BIC (ΔBIC) was calculated by subtracting the BIC value of the combined model from the single Voigt model. The BIC is an indicator that evaluates the goodness of a model, taking into account how well the model fits the data and the complexity of the model. The formula for BIC is as follows:

$$BIC = -2 \ln L^* + k \ln n \quad (3)$$

where L^* is the maximum likelihood calculated from the likelihood of the observed spectrum and the model function optimized results, n is the number of data points in the spectrum, and k is the number of parameters in the model function. Assuming that the noise for each data point in the spectrum follows a Gaussian distribution with variance σ^2 , the likelihood is given by:

² The quiescent state spectra are the averaged spectra of the quiescent state. The quiescent state is defined as the state immediately before any significant increase in brightness was observed. If data from this pre-flare quiescent state were missing, the post-flare state was used as the quiescent state.

$$L = \prod_{i=1}^n \frac{1}{\sqrt{2\pi\sigma^2}} e^{-\frac{(y_i - f(x_i))^2}{2\sigma^2}} \quad (4)$$

where y_i is the y-axis value (Diff. Intensity) of the data in the observed spectrum, and $f(x_i)$ is the corresponding y-axis value in the model spectrum (see Figure 2 (b)). Furthermore, the maximum log-likelihood is calculated as:

$$\ln L^* = -\frac{n}{2} \ln(2\pi\sigma^2) - \frac{n}{2} \quad (5)$$

$$\sigma = \sqrt{\frac{1}{n} \sum_{i=1}^n (y_i - f(x_i))^2} \quad (6)$$

The criterion for determining asymmetry was set when ΔBIC was greater than 2 for at least two consecutive points. This is because if $\Delta\text{BIC} > 0$, the combined model is statistically significantly better than the single Voigt model, and a $\Delta\text{BIC} > 2$ indicates a significant difference between the two models (Fabozzi et al. 2014). To exclude influences such as cosmic rays, the criterion was set to require $\Delta\text{BIC} > 2$ for at least two consecutive points. If the center of the Gaussian function in the combined model was on the shorter wavelength side of the $\text{H}\alpha$ line center, it was determined to be a blue asymmetry. If it was on the longer wavelength side, it was determined to be a red asymmetry.

After the identification of asymmetries, in order to accurately measure the velocity and amplitude with the same method as the previous study, extraction of the redshifted and blueshifted components was conducted by following Maehara et al. (2021); Namizaki et al. (2023). First, in order to extract the symmetric line center components (referred to as “flare components”), we fitted a Voigt function to the differential spectrum during the flare duration (brown solid line in Figure 2 (c)). Unlike the fitting for BIC calculation (see Figure 2 (b)), the fitting was applied only to the parts on the longer or shorter wavelength side of the $\text{H}\alpha$ line center, so that the fitting was not affected from blueshifted or redshifted components, respectively. Additionally, the center of the Voigt function was fixed at the $\text{H}\alpha$ line center. Then, the flare components obtained from the fit was subtracted from the observed data. In this study, the resulting residuals were defined as the ‘blueshift/redshift components’ (navy cross in Figure 2 (c)). These residuals were then fitted with a Gaussian function (purple dotted line in Figure 2 (c)), and the Doppler velocity corresponding to the center of the fitted Gaussian function was estimated as the blueshift/redshift velocity. At this time, the width σ of the Gaussian function was set to be at least half the wavelength resolution during the fitting. Additionally, the equivalent widths of the central and asymmetric components were calculated by integrating along the wavelength within a ± 15 Å range from the center for the Voigt and Gaussian fits, respectively. Doppler velocity corresponding to the center of the fitted Gaussian function was estimated as the blueshift/redshift velocity.

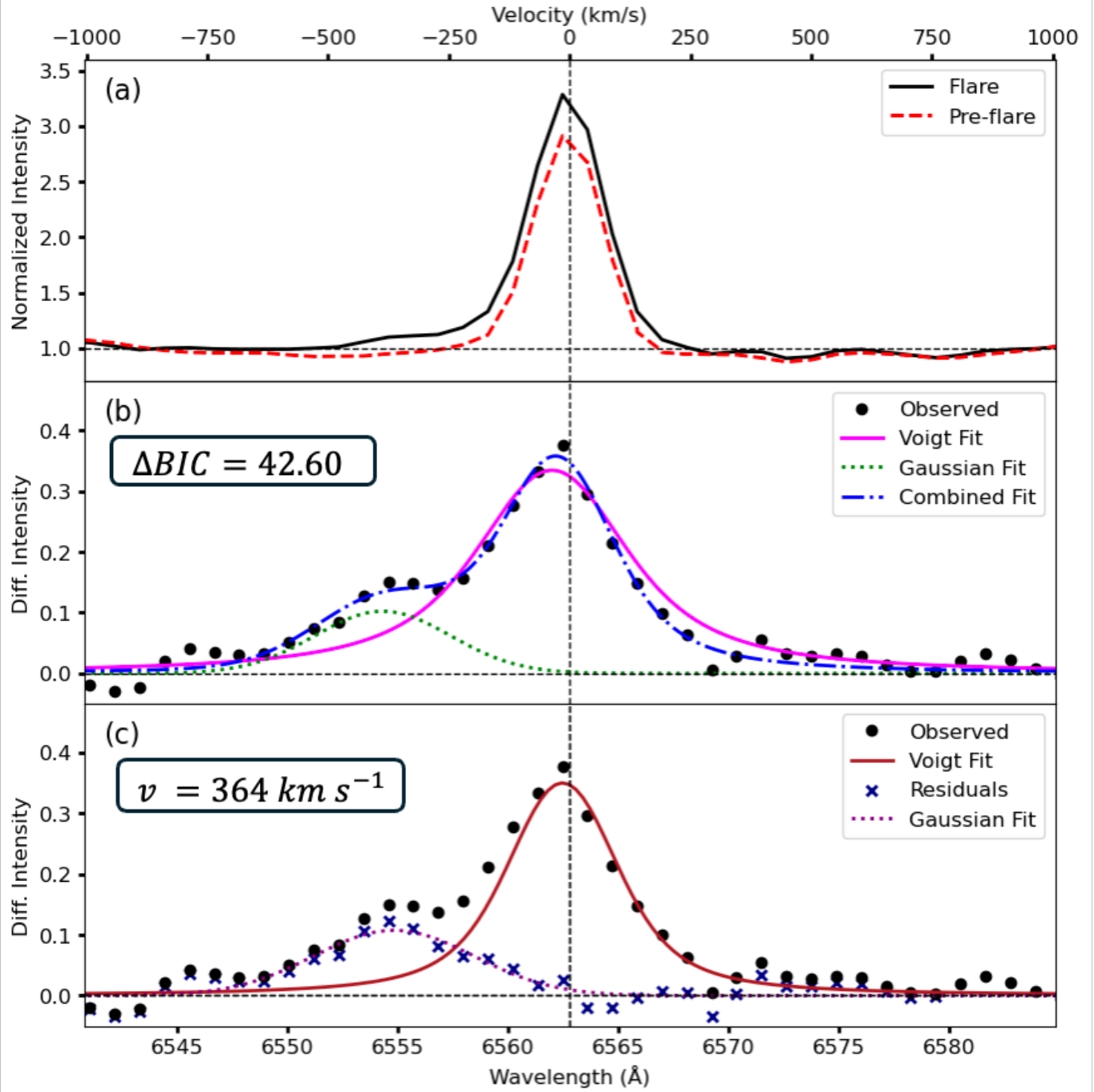


Figure 2. Example of normalized spectra and differential spectra. The lower axis represents the wavelength, and the upper axis shows the Doppler velocity relative to the H α line (6562.8 Å). The vertical dashed lines indicate the center wavelength of the H α line. (a) Example of normalized spectra. The black solid line shows the H α line spectrum normalized by the continuum spectrum during the flare period. The red dashed line shows the H α line spectrum normalized by the continuum spectrum in the pre-flare period. (b) Example of differential spectrum fitting for asymmetry determination. Black dots represent observational data and the blue dash-dotted line represents the fit by the combination of Voigt (magenta solid line) and Gaussian (green dotted line) functions. The value in the top left indicates the ΔBIC value for this differential spectrum. (c) Example of differential spectrum fitting for the extraction of blueshifted components. Black dots represent the observational data. The brown solid line represents the Voigt function fitted to the components at longer wavelengths than the H α line center. The navy crosses represent the residuals of the Voigt function (brown solid line) from the observational data (black dots). The dashed black lines represent the Gaussian functions fitted to these residuals (navy crosses).

Table 2. List of H α Flares

ID ^a	Date	Start_BJD ^b	$\tau_{H\alpha}$ (min) ^c	$E_{H\alpha}$ (erg) ^d	E_{flare} (erg) ^e	τ_{flare} (min) ^f	Completeness ^g	WL/NWL ^h	Asymmetry ⁱ
Y1	2021 Jan 18	2459233.2613	17	5.0×10^{29}	-	-	complete	NWL	symmetry
Y2	2021 Jan 19	2459234.1601	21	8.4×10^{29}	-	-	complete	NWL	symmetry
Y3	2021 Jan 19	2459234.1851	37	1.3×10^{30}	1.5×10^{31}	9.7	complete	WL	symmetry
Y4	2021 Jan 24	2459238.9382	319	3.8×10^{32}	1.2×10^{34}	235.3	complete	WL	redshift
Y5	2021 Jan 25	2459239.9288	51	4.2×10^{30}	2.5×10^{32}	39.0	incomplete	WL	redshift
Y6	2021 Jan 25	2459240.0683	36	2.3×10^{30}	5.8×10^{30}	2.7	complete	WL	redshift
Y7	2021 Jan 25	2459240.1479	30	1.8×10^{30}	4.0×10^{31}	15.0	complete	WL	symmetry
Y8	2021 Jan 28	2459243.1830	18	2.2×10^{30}	8.2×10^{31}	13.0	complete	WL	blueshift
Y9	2021 Jan 29	2459244.1436	23	9.0×10^{29}	-	-	complete	NWL	symmetry
Y10	2021 Jan 29	2459244.2578	17	7.2×10^{29}	-	-	complete	NWL	symmetry
Y11	2021 Jan 30	2459245.0639	14	6.1×10^{29}	-	-	complete	NWL	symmetry
Y12	2021 Jan 30	2459245.0925	137	9.8×10^{30}	-	-	complete	NWL	blueshift
Y13	2021 Jan 31	2459245.9846	49	1.6×10^{30}	-	-	complete	NWL	symmetry
Y14	2021 Jan 31	2459246.0258	8	1.7×10^{29}	-	-	complete	NWL	symmetry
Y15	2021 Jan 31	2459246.0615	28	6.0×10^{29}	-	-	complete	NWL	symmetry
Y16	2021 Jan 31	2459246.1187	146	9.2×10^{30}	1.9×10^{31}	8.0	complete	WL	redshift
Y17	2021 Feb 2	2459247.9109	26	1.5×10^{30}	-	-	complete	NWL	symmetry
Y18	2021 Feb 2	2459247.9538	10	5.9×10^{29}	-	-	complete	NWL	symmetry
Y19	2021 Feb 2	2459247.9681	17	4.1×10^{29}	-	-	complete	NWL	symmetry
Y20	2021 Feb 2	2459247.9806	192	1.2×10^{31}	-	-	complete	NWL	blueshift

Table 2. (*continued*)

ID ^a	Date	Start_BJD ^b	$\tau_{H\alpha}$ (min) ^c	$E_{H\alpha}$ (erg) ^d	E_{flare} (erg) ^e	τ_{flare} (min) ^f	Completeness ^g	WL/NWL ^h	Asymmetry ⁱ
Y21	2021 Feb 3	2459248.9709	122	2.8×10^{31}	4.3×10^{32}	72.3	incomplete	WL	redshift
Y22	2021 Feb 3	2459249.0835	45	2.3×10^{30}	-	-	complete	NWL	symmetry
Y23	2021 Feb 3	2459249.1247	90	5.2×10^{30}	4.7×10^{30}	1.7	complete	WL	symmetry
Y24	2021 Feb 3	2459249.1953	30	1.2×10^{30}	-	-	complete	NWL	symmetry
Y25	2021 Feb 4	2459249.9659	61	2.0×10^{30}	-	-	complete	NWL	symmetry
Y26	2021 Feb 4	2459250.0240	82	3.8×10^{30}	-	-	complete	NWL	symmetry
Y27	2021 Feb 4	2459250.1054	124	7.4×10^{30}	6.6×10^{31}	20.0	complete	WL	symmetry

^a Label of H α flares^b Start time of H α flares (BJD)^c Duration of H α flares (min)^d Energy of the H α flare (erg)^e Bolometric flare energy (erg)^f Duration of white-light flares (min)^g Completeness. “complete” indicates a flare that was fully observed from before the flare onset to the quiescent state after the flare, “incomplete” indicates a flare missing some data during the flare event.^h Classification of white-light/non-white-light flares. “WL” indicates white-light flares detected in Section 3.1, “NWL” indicates non-white-light flares that were detected in the H α light curve but not in the TESS light curve.ⁱ Classification of asymmetry based on Section 3.3. “symmetry” indicates flares with no asymmetry, “redshift” indicates flares with red asymmetry, and “blueshift” indicates flares with blue asymmetry.

4. RESULTS

4.1. Detection of $H\alpha$ and white-light flares

Following the methodology described in Section 3.2, a total of 27 $H\alpha$ flares were detected. The energy $E_{H\alpha}$ and duration of the detected $H\alpha$ flares $\tau_{H\alpha}$ are listed in Table 2. The $H\alpha$ flare energy $E_{H\alpha}$ ranges from 1.7×10^{29} to 3.8×10^{32} erg, and the duration ranges from 8 to 319 minutes, respectively. The total observation time with the Seimei Telescope from January 14 to February 8, 2021, was 2.8 days. The frequency of detectable $H\alpha$ flares with $E_{H\alpha} > 1.0 \times 10^{29}$ erg is approximately 10 events per day.

Using the methods outlined in Section 3.1, 130 white-light flares were detected. The upward arrows in Figure 1(a) indicate the start times of the detected white-light flares. The bolometric energy E_{flare} and the duration τ_{flare} of the white-light flares corresponding to the detected $H\alpha$ flares are listed in Table 2. The bolometric energy E_{flare} ranges from 4.7×10^{30} to 1.2×10^{34} erg, and the duration ranges from 1.7 to 235.3 minutes, respectively. The total observation time with TESS from January 14 to February 8, 2021, was 23.5 days. As a result, the frequency of the detectable white-light flares is estimated to be 5.5 events per day. The occurrence frequency of $H\alpha$ flares is higher than that of white-light flares, with only 10 out of 27 $H\alpha$ flares associated with white-light flares. There is not necessarily a one-to-one correspondence between $H\alpha$ and white-light flares. $H\alpha$ flares are not necessarily accompanied by white-light flares. This phenomenon, termed “non-white-light flare”, has been reported in both solar contexts (Watanabe et al. 2017) and stellar contexts (Namekata et al. 2020).

4.2. Determination of $H\alpha$ Line Asymmetry

Among these 27 $H\alpha$ flares detected in this study, five (Y4, Y5, Y6, Y16, Y21) show red asymmetries, and three (Y8, Y12, Y20) show blue asymmetries, as listed in Table 2. The method described in Section 3.3 was used for the identification of asymmetries. Figures 3 – 10 show the light curves and temporal changes in the $H\alpha$ line profiles for the flares determined to show blue/red asymmetries. Specifically, Figure 3 corresponds to flare Y4, Figure 4 to Y5, Figure 5 to Y6, Figure 8 to Y16, and Figure 10 to Y21, which exhibit red asymmetries. For blue asymmetries, Figure 6 corresponds to flare Y8, Figure 7 to Y12, and Figure 9 to Y20. Other events for which asymmetries were not detected are shown in Appendix B. The maximum velocities $v_{\text{asym,max}}$ and duration of asymmetry τ_{asym} for these asymmetric components are shown in Table 3. For red asymmetry, $v_{\text{asym,max}}$ ranges from 188 to 400 km s^{−1}, and τ_{asym} ranges from 6 minutes to 319 minutes. For blue asymmetry, $v_{\text{asym,max}}$ ranges from 202 to 445 km s^{−1}, and τ_{asym} ranges from 8 minutes to 160 minutes. We evaluated the error of $v_{\text{asym,max}}$ based solely on the Gaussian fitting error. The variation in the observed velocity solution during observations is around 1–2 km s^{−1} and this value is sufficiently small compared to the fitting error as explained in Appendix A. It should be noted that measured velocities $v_{\text{asym,max}}$ are projected ones. The actual values might be higher than that, depending on the configuration. Each blue and redshift event shows very various properties in velocity, duration, and its spectral behavior. Not all of these events are discussed in this paper, but we discuss the blueshift events in the following Section 5.2, and one transient redshift event (Y6) in Section 5.3 in detail.

5. DISCUSSION

5.1. Discovery and Implication of Rapid, Short-Duration Red/Blue Asymmetries

Since the advantage of this study is the high time cadence observation, we first compare the durations of red/blue asymmetries detected in this study with previous studies. Figure 11 shows histograms of the duration of (a) blue asymmetries and (b) red asymmetries during M-dwarfs flares detected in this study, as well as those reported in previous studies. Additionally, Table 4 lists the events from previous studies displayed in Figure 11. From Figure 11, previous studies have only reported asymmetries lasting longer than 20 minutes. We found that the asymmetries during flares Y6 and Y8 in this study are with duration of 6 and 8 minutes, respectively. This is likely due to the ~5-min or longer temporal resolution of observations in previous studies (e.g., Vida et al. 2016; Honda et al. 2018; Maehara et al. 2021; Wu et al. 2022; Wollmann et al. 2023; Notsu et al. 2024; Inoue et al. 2024), which are not sufficient to detect short-duration asymmetries. M-dwarfs have stronger surface gravity compared to G-type or K-type dwarfs, and they could decelerate high-velocity (~350 km s^{−1}) plasma to below 100 km s^{−1} within approximately 5 minutes. In the following sections, we discuss a physical interpretation of the short-duration blueshift in Section 5.2 and the short-duration redshift in Section 5.3.

5.2. Origins of Blue Asymmetry

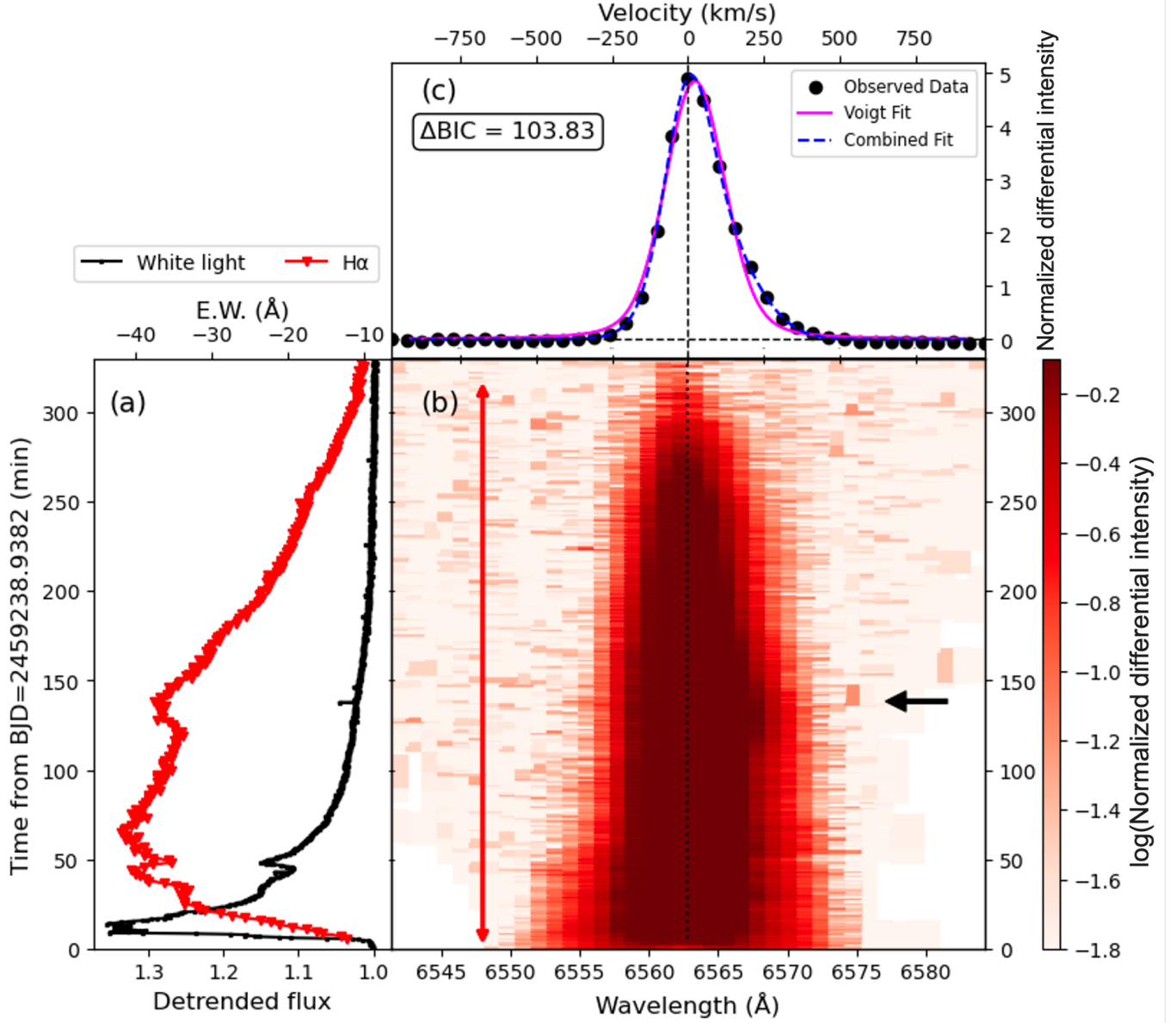


Figure 3. (a) Light curves of white light and H α line for flare Y4. The black solid line represents the detrended light curve of the white light emission showing long-term variations, and the red solid line represents the light curve of the H α line. The left vertical axis represents the detrended flux (F/F_{star}), and the right vertical axis represents the equivalent width of the H α line. (b) Temporal evolution of the H α line profile for Y4. The left vertical axis represents the wavelength, and the right vertical axis shows the Doppler velocity relative to the central wavelength of H α (6562.8 Å). The horizontal axis represents the elapsed time (min) from the start of the flare, with BJD=2459238.9382 as the reference point. The color bar indicates the logarithm of the normalized intensity in the differential spectrum. Black arrows mark the time of maximum ΔBIC , and red bidirectional arrows indicate the duration of red asymmetry. (c) Differential spectrum at the time of maximum ΔBIC . The lower axis represents the wavelength, and the upper axis shows the Doppler velocity relative to the H α line (6562.8 Å). The vertical axis represents the differential intensity, with vertical dotted lines indicating the central wavelength of H α , and horizontal dotted lines indicating the zero position of the differential intensity. Black dots represent observational data, the magenta solid line represents a fit by a Voigt function, and the blue dashed line represents a fit by a combination of Voigt and Gaussian functions. The value in the top left indicates the ΔBIC value for this differential spectrum.

Table 3. Flares showing red/blue asymmetry

ID ^a	Asymmetry ^b	WL/NWL ^c	$v_{\text{asym,max}}$ (km s ⁻¹) ^d	τ_{asym} (min) ^e	$\Delta\text{BIC}_{\text{max}}$ ^f	$\tau_{H\alpha}$ (min) ^g	$E_{H\alpha}$ (erg) ^h	Figure ⁱ
Y4	redshift	WL	402 ± 47	319	114.31	319	3.8×10^{32}	Figures 3
Y5	redshift	WL	265 ± 21	35	8.50	51	4.2×10^{30}	Figures 4
Y6	redshift	WL	295 ± 12	6	15.62	36	2.3×10^{30}	Figures 5
Y8	blueshift	WL	445 ± 36	8	42.60	18	2.2×10^{30}	Figures 6
Y12	blueshift	NWL	254 ± 43	14	14.14	137	9.8×10^{30}	Figures 7
Y16 _a	redshift	WL	242 ± 32	66	15.26	146	9.2×10^{30}	Figures 8
Y16 _b	redshift		223 ± 21	35	5.05			
Y20	blueshift	NWL	202 ± 18	160	30.88	192	1.2×10^{31}	Figures 9
Y21	redshift	WL	188 ± 27	98	18.41	122	2.8×10^{31}	Figures 10

^a Label of the H α flare^b Classification of asymmetry based on Section 3.3. “symmetry” indicates flares with no asymmetry, “redshift” indicates flares with red asymmetry, and “blueshift” indicates flares with blue asymmetry.^c Classification of white-light/non-white-light flares. “WL” indicates white-light flares detected in Section 3.2, “NWL” indicates non-white-light flares that were not detected.^d Maximum velocity of the asymmetrical component (km s⁻¹) measured by the fitting process (see Section 3.3).^e Duration of asymmetry (min)^f Maximum ΔBIC value^g Duration of the H α flare (min)^h Energy of the H α flare (erg)ⁱ Corresponding Figures showing the light curve and dynamic spectrum.

5.2.1. Interpretations of blue asymmetry

In this section, we discuss the origins of blueshift events. The origins of blue asymmetries can be attributed to three possible phenomena: prominence eruptions (e.g., Otsu et al. 2022), chromospheric evaporation associated with upflows of cool plasma (chromospheric upflows) (e.g., Tei et al. 2018), and redshift absorption due to post-flare loops (e.g., Honda et al. 2018; Otsu et al. 2022). In the following, we discuss these three interpretations based on solar observations and models of M-dwarfs.

First, in solar flares, cool upflows on the chromospheric evaporations are indicated from the blue asymmetry of the chromospheric lines with a velocity of around a few 10 km s⁻¹ (Švestka et al. 1962; Tei et al. 2018; Li et al. 2019; Huang et al. 2019). The typical duration of observable blueshift in chromospheric lines is just a few minutes at a given footpoint (Tei et al. 2018; Li et al. 2019; Huang et al. 2019), but its total duration could be longer if we see the multiple flare loops in the Sun-as-a-star view. Allred et al. (2006) performed 1D numerical radiative hydrodynamic simulation for flaring M-dwarf atmosphere and showed that the possible cool upflows with a velocity of ~ 50 km s⁻¹ can be formed above the hot evaporation flow as a result of the injection of high energy electron beams into deep chromosphere. This is thought to be one of the causes of the blue asymmetries in M-dwarf flares.

Second, in solar flares, the downward flow of post-flare loops occurring in the late phase of the flare exhibits red wing absorption in the H α line. The typical velocity of this flow ranges from several tens of km s⁻¹ to 100 km s⁻¹, and the duration exceeds 60 minutes (e.g., Liu et al. 2013; Song et al. 2016; Otsu et al. 2022). Honda et al. (2018) reported a blue asymmetry caused by red wing absorption in the H α line exhibited in the late phase of M-dwarf flares. This suggests the downward flow of post-flare loops. In M-dwarfs, the background continuum intensity is much cooler than that of the Sun. Therefore, it is unclear whether the post-flare loop can be seen in emission or absorption in the H α line. While the model presented in Wollmann et al. (2023) suggests that such phenomena are visible in emission, this is also dependent on various parameters and they are not yet fully understood. Therefore, further modeling is necessary.

Third, regarding prominence eruptions, in both the Sun and solar-type stars, these events are observed as H α absorption on the disk and as emission outside the limb (Otsu et al. 2022; Namekata et al. 2022; Namekata et al. 2024). On the other hand, Leitzinger et al. (2022) showed that prominence eruption on the disk of M-dwarfs can also be observed as H α emission using 1D NLTE modeling and cloud model formulation. Therefore, in M-dwarfs, prominence eruptions on the disk and outside the limb might be observed as H α emission. The velocity of prominence eruptions on the Sun ranges from several tens of km s⁻¹ to several hundreds of km s⁻¹ (Gopalswamy et al. 2003; Seki et al. 2021).

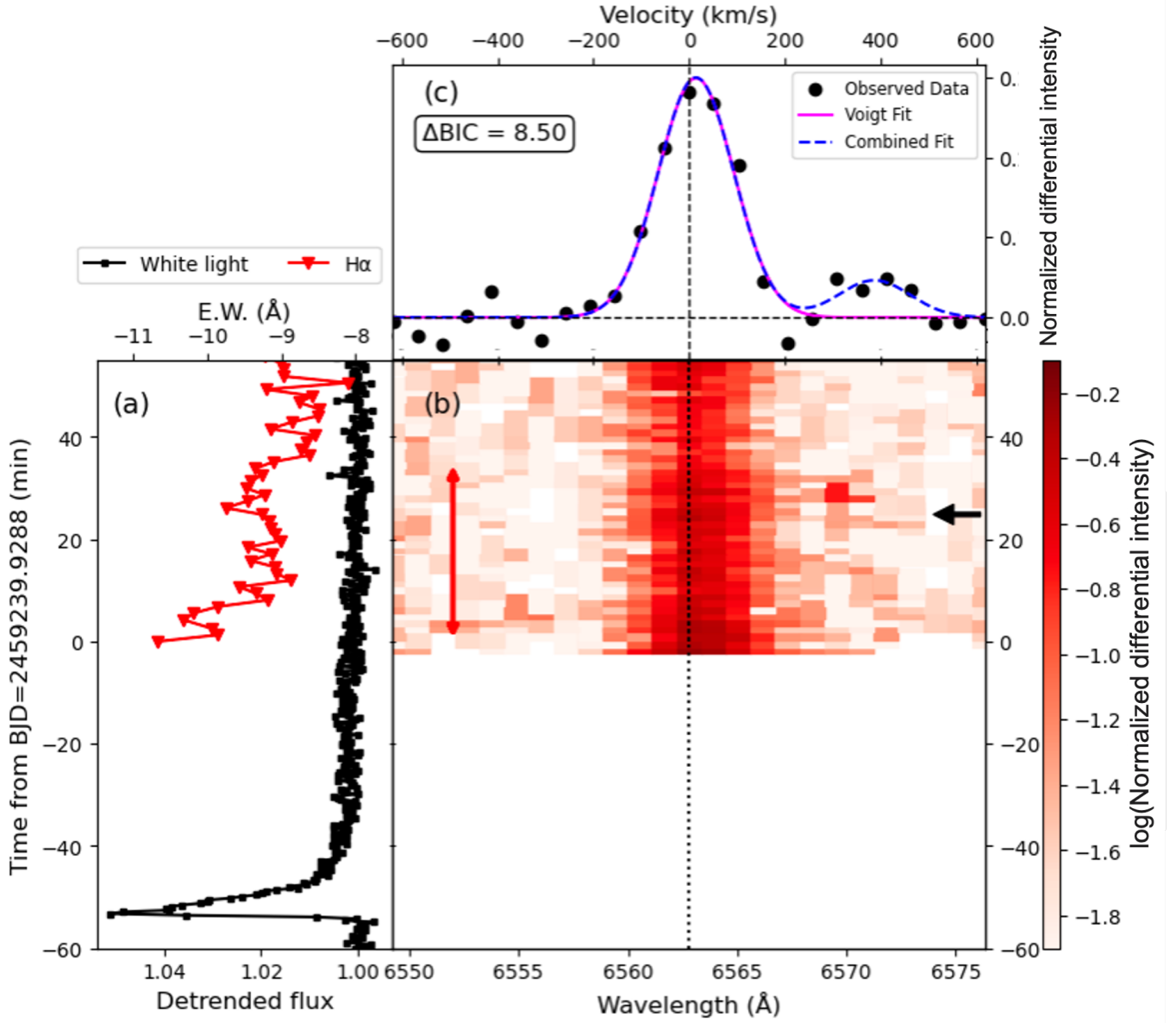


Figure 4. The same as Figure 3, but for the event of Y5.

These three scenarios might be difficult to distinguish based solely on snapshot spectra. However, the data available for this study were observed with an unprecedented temporal resolution of one minute and are further complemented by comprehensive optical photometric observations from TESS for all events. The TESS white-light flare data, which can have significant constraints on the emission from flare ribbons, can help distinguish flare emissions from other possibilities. Using these high-temporal-resolution photometric and spectroscopic data could enhance our ability to constrain the origins of blue asymmetries. The following sections explore the causes of the three blue asymmetries (Y8, Y12, and Y20), comparing with observations of the Sun and models of M-dwarfs.

5.2.2. Flare Y8: Rapid, Short-Duration Blue Asymmetry

In this section, we discuss the origin of the blue asymmetry during the flare Y8 that occurred on 2021 January 28. We first summarize the observational results for the flare Y8. Figure 6 shows the dynamic spectrum of the Y8 event. Also, Figure 12 shows the time evolution of the equivalent width of the flare component and the blueshifted

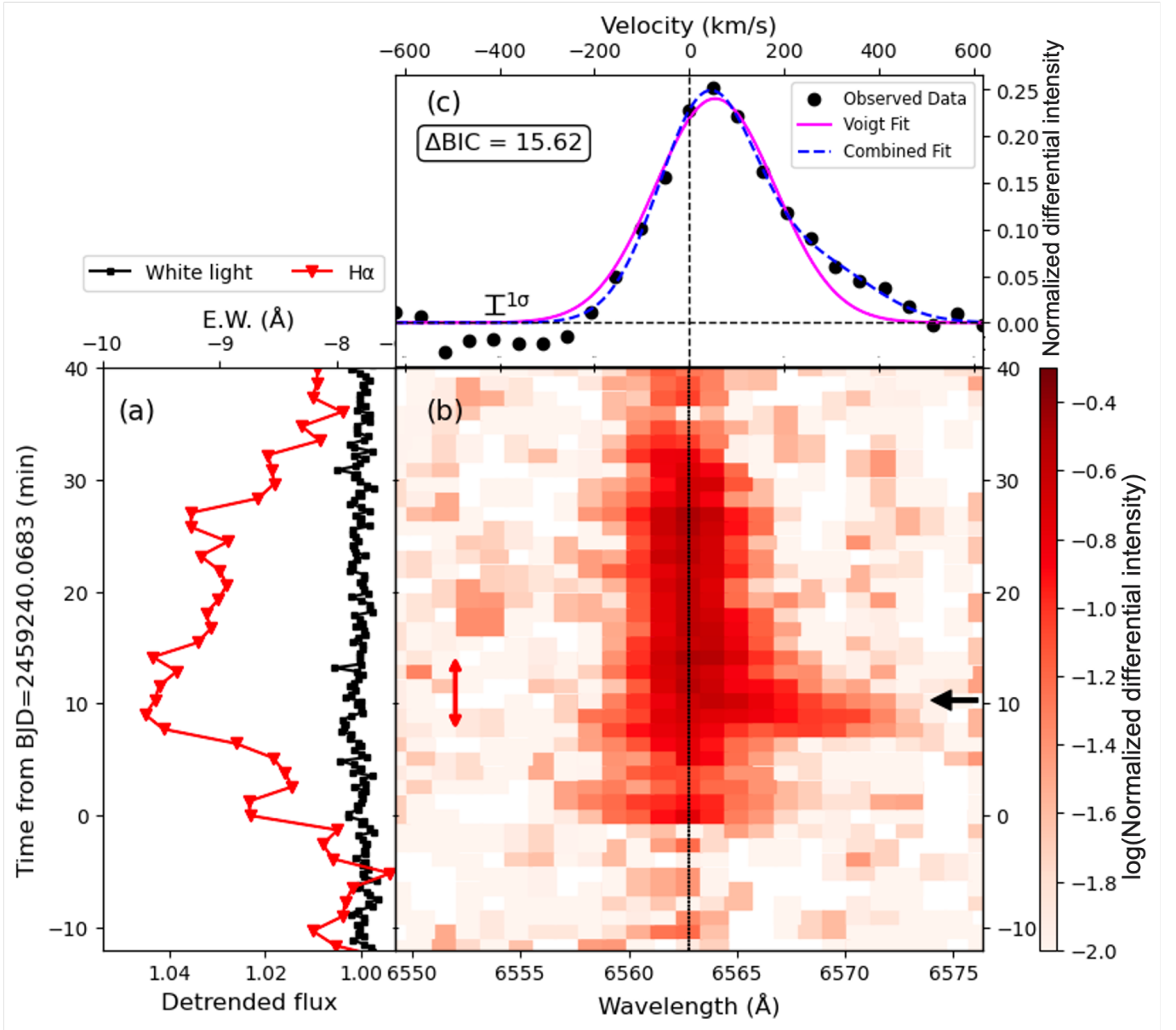


Figure 5. The same as Figure 3, but for the event of Y6. The continuum seems weird on the blue side, but it's within the range of the noise level.

component, and 6 (d) shows the time evolution of the velocity of the blueshifted component. As shown in Table 3, the maximum velocity of these blueshifted components was $445 \pm 36 \text{ km s}^{-1}$, and the duration of asymmetry was 8 minutes. This velocity is relatively high among typical blueshifted components measured using the same method in time-resolved observations of M-dwarf flares. ($\sim 100 \text{ km s}^{-1}$, e.g., Honda et al. 2018; Maehara et al. 2021; Notsu et al. 2024; Inoue et al. 2024). Vida et al. (2019) investigated more than 5500 snapshot spectra of chromospheric lines of M-dwarfs, and reported that 478 spectra among them showed line asymmetries. The typical maximum velocities for blueshifted components of these spectra are 100–300 km s^{-1} , but these maximum velocities were defined as the point where the residual profile merges with the continuum. As a corresponding velocity to be compared with these maximum velocities of 100–300 km s^{-1} in Vida et al. (2019), the maximum value of the central Gaussian velocity plus the Gaussian line width σ of flare Y8 is around $\sim 550 \text{ km s}^{-1}$. Additionally, as discussed in Section 5.1, the duration of this event is the shortest among H α blueshift events reported in publications.

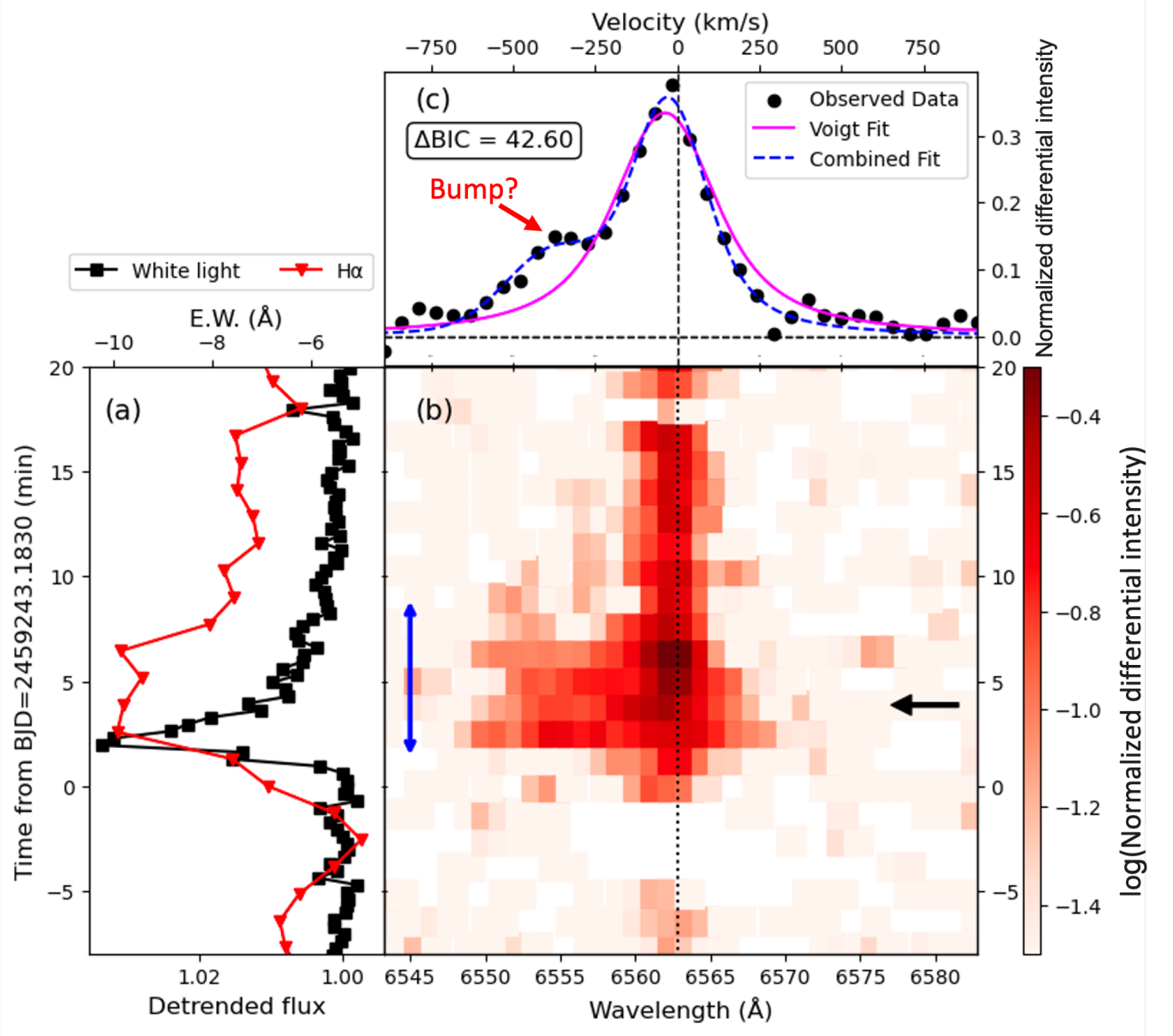


Figure 6. The same as Figure 3, but for the event of Y8. In this case, blue bidirectional arrows indicate the duration of blue asymmetry.

In addition to the central Gaussian velocity, we here mention the velocity dispersion for each event Y6, Y8, and Y20. As we described above, the observed maximum velocities of these events are below the escape velocity of YZ CMi. However, these blueshifted components are broadened more than velocity resolution $\sim 70 \text{ km s}^{-1}$ (Matsubayashi et al. 2019). In Figure 12 and Figure 13 (d), the navy diamonds indicate the evolution of the central velocity plus the Gaussian line width σ . Similarly, in Figure 15 (d), the brown diamonds show the same evolution. This can be interpreted as the velocity distribution of the expanding prominence (Namekata et al. 2024). Based on this interpretation, we can assume that the width plus central velocity can be regarded as the maximum velocity component of the eruptive prominence.

Here we discuss the possible origin of this blue asymmetry. The typical velocities of chromospheric upflows observed in solar flares (about a few 10 km s^{-1} for solar observation; Tei et al. 2018; $\sim 50 \text{ km s}^{-1}$ for M-dwarf flare modeling; Allred et al. 2006) are much smaller than the maximum velocity of the observed blueshifted components. This suggests that chromospheric upflows are unlikely to be the cause. Next, Figure 6 (c) shows that the line profile exhibits the expanded “bump-like shape” centered at approximately -400 km s^{-1} , corresponding to a separate emission peak profile

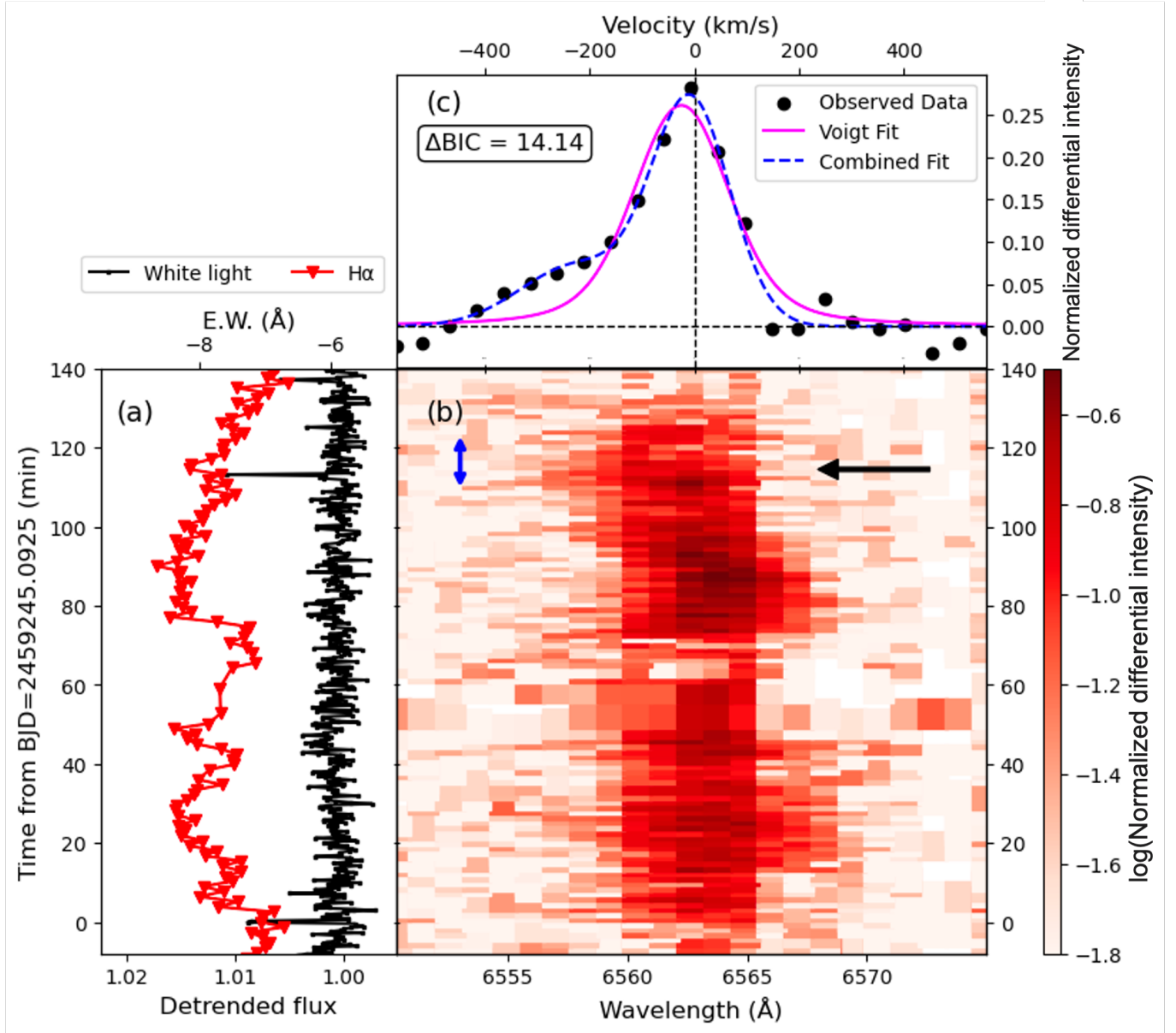


Figure 7. The same as Figure 6, but for the event of Y12.

distinct from the H α line center. This shape cannot be solely explained by redshift absorption from the post-flare loop because the red wing absorption itself cannot make the bump-like feature in the blue wing. On the other hand, as we described before, prominence eruptions can be observed as blueshifted emissions in M-dwarfs. Therefore, they may make the bump-like feature in the blue wing. The maximum velocity of $445 \pm 36 \text{ km s}^{-1}$ in this event is relatively fast but almost within the typical velocity of solar prominence eruptions ($10\text{--}400 \text{ km s}^{-1}$; [Gopalswamy et al. 2003](#); [Seki et al. 2021](#)). Both in terms of velocity and profile shape, the characteristics of the prominence are consistent. Therefore, this blueshifted component is highly likely to indicate a prominence eruption.

Figures 12 (a) and (d) show that this blueshifted component appeared simultaneously with the white-light flare, and the acceleration almost finished before or just after the peak of the white-light flare, followed by almost constant velocity for about 6 minutes. This is consistent with solar observations where the eruptions are mainly accelerated within the impulsive phase of flares ([Aschwanden 2021](#)). This also supports the possibility of a prominence eruption.

5.2.3. Flare Y12: Delayed Blue Asymmetry

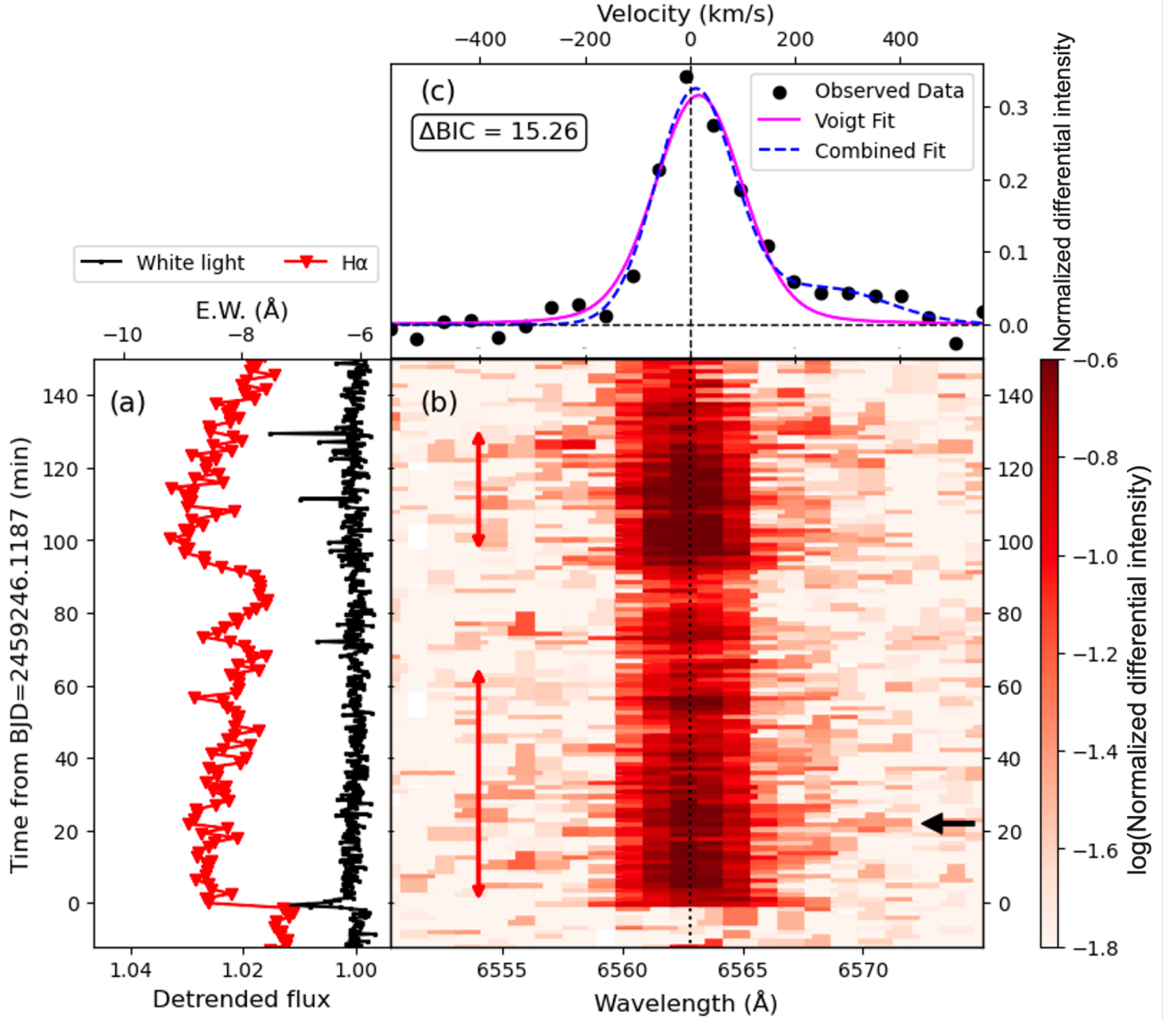


Figure 8. The same as Figure 3, but for the event of Y16.

In regard to the blue asymmetry during the flare Y12 on 2021 January 30, Figure 7 shows the dynamic spectrum. Figure 13 (d) shows the time evolution of the blueshifted component with the maximum velocity of 254 km s^{-1} and the duration of 14 minutes. Figure 13 (d) shows the blueshifted component accelerates and reaches its peak approximately 4 minutes after its appearance and then decelerates at a roughly constant rate, with a deceleration that is ~ 0.5 times the surface gravity. This flare lacks a significant white-light flare emission, classified as a non-white-light flare (Figure 13). The corresponding H α flare shows a complex light curve with several peaks and a long duration of 136 minutes, probably meaning a superposition of several flares. The blueshift event appears in the final phase of this series of flares with a potential H α peak. There is a corresponding white-light spike with an amplitude of approximately 0.01 associated with blue asymmetry in TESS light curve (Figure 13), but it was not judged as a flare in our flare detection algorithm because it does not have more than three consecutive points. During the series of the flares, we can see possible red asymmetry, e.g., in 80–100 min, as in Figure 7, but it was not significant based on the BIC threshold.

By following the same discussion as in Section 5.2.2, the relatively high velocity of the blue asymmetry simply suggests that this blueshifted component is likely to indicate a prominence eruption. The almost constant deceleration,

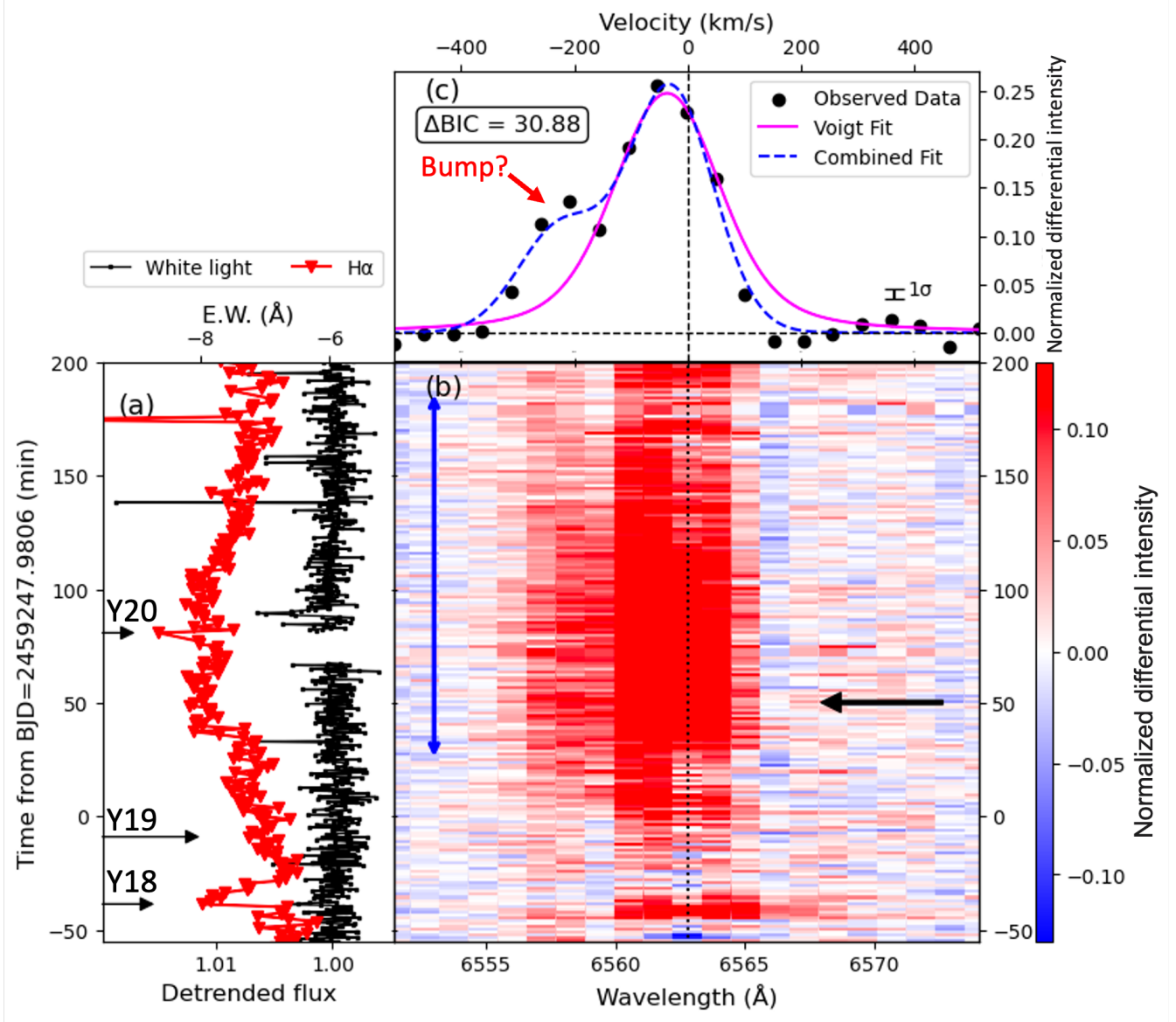


Figure 9. The same as Figure 6, but for the event of Y20. Unlike the others, the color bar indicates the normalized intensity in the differential spectrum, including negative values.

approximately 0.5 times the surface gravity, may suggest either the free fall of a prominence eruption that occurred at the limb and erupted at an angle of 60 degrees from the line of sight, or a prominence eruption that occurred at a height of $1.4 R_{\text{star}}$ above the disc. The interesting point is that this blue asymmetry is seen in the latter half of a series of Hα flares, following a possible red asymmetry. As shown in Figures 7 (a) and 13 (b), this blue asymmetry appears approximately 40 minutes after the Hα flare peak at $t \sim 75$ min. This delayed blue asymmetry is similar to the event reported by Inoue et al. (2024). Inoue et al. (2024) reported a blue asymmetry that occurred approximately 1 hour after the Hα flare peak, and this delay time is comparable to this event. Blue asymmetries of stellar flares are reported to begin to appear around at the peak of flares (e.g., Vida et al. 2016; Honda et al. 2018; Maehara et al. 2021; Notsu et al. 2024), so this kind of delayed case is relatively rare. Inoue et al. (2024) proposed that the delay in this blue asymmetry could be due to (i) another flare/prominence eruption occurring in the decay phase (e.g., Zirin 1969; Mason et al. 2021 for solar observations) or (ii) a prominence erupted during the decay phase of the flare (e.g., Kurokawa et al. 1987 for solar observations). Figure 13 (b) shows the increase in the equivalent width of the Hα line center component at the onset of the blue asymmetry can be observed at $t \sim 115$ min. This suggests that this blue

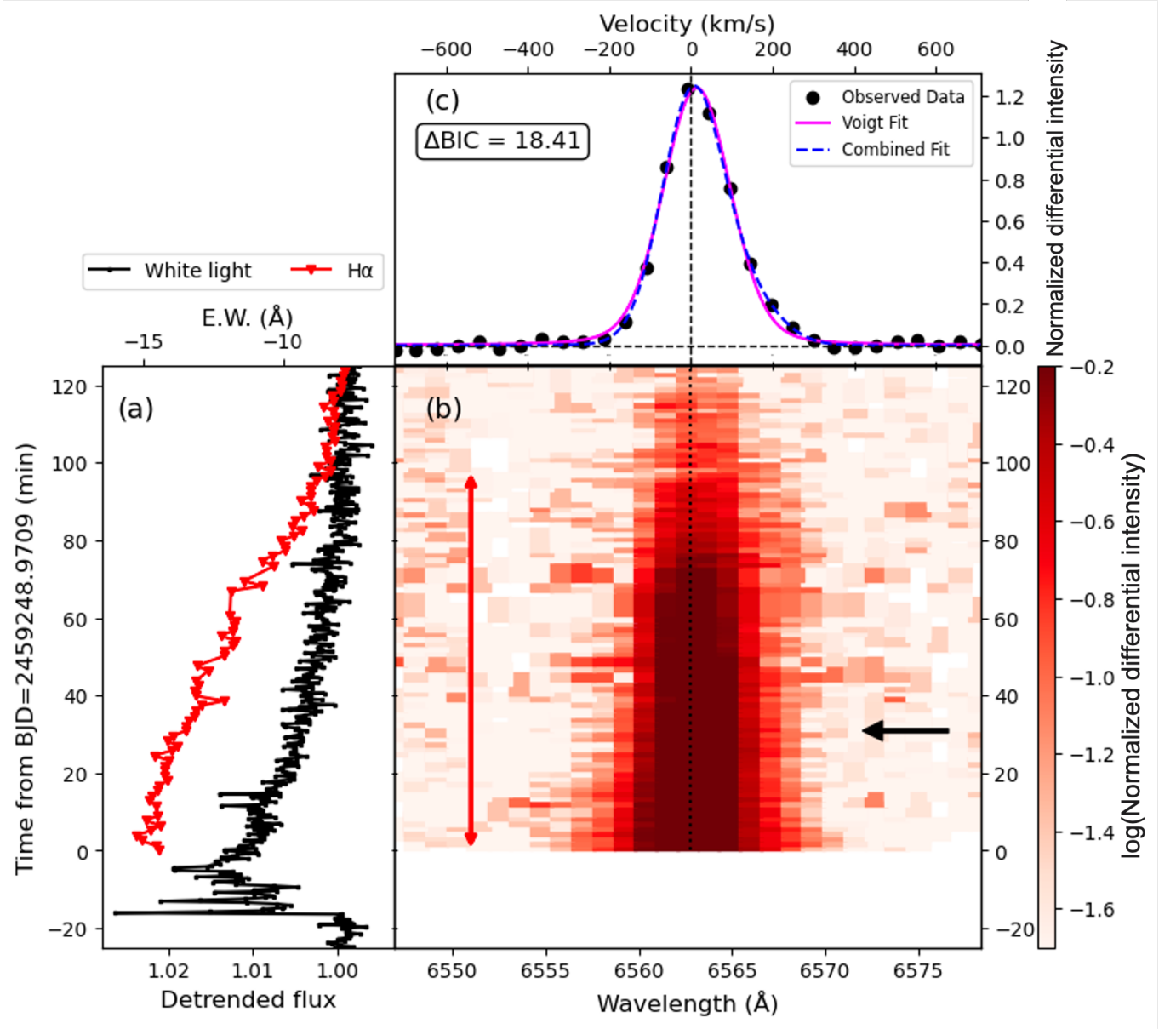


Figure 10. The same as Figure 3, but for the event of Y21.

asymmetry may be associated with a prominence eruption triggered by another flare in the latter half of the duration of flare Y12. Therefore, we cannot distinguish these two possibilities for this event as well.

In addition to these interpretations, the possible red asymmetry ($\Delta\text{BIC} \sim 0$) that was below the BIC threshold ($\Delta\text{BIC} > 2$) before the blueshift is not accompanied by significant white-light flare. This may suggest the occurrence of backward eruptions around the stellar limb (see Section 5.3). The later blueshift could indicate falling material. On the other hand, the velocity during the blue asymmetry accelerates initially and then decelerates at a roughly constant rate. These velocity changes cannot be explained by backward eruptions because the blueshifted velocity should increase as the material falls.

5.2.4. Flare Y20: Long-Duration Blue Asymmetry

In regard to the blue asymmetry during the flare Y20 on February 2, Figure 9 shows the dynamic spectrum. Figure 14 (b) shows that before Y20, there are consecutive flares, the impulsive H α flare Y18 and the gradual H α flare

Table 4. Summary of asymmetry durations in prior research

Asymmetry	Duration (min)	Star Name	Reference
blueshift	24	V374 Peg	Vida et al. (2016)
blueshift	24	V374 Peg	Vida et al. (2016)
blueshift	36	V374 Peg	Vida et al. (2016)
blueshift	120	EV Lac	Honda et al. (2018)
blueshift	60	YZ CMi	Maehara et al. (2021)
blueshift	45	EV Lac	Inoue et al. (2024)
blueshift	20	YZ CMi	Notsu et al. (2024)
blueshift	20	YZ CMi	Notsu et al. (2024)
blueshift	100	YZ CMi	Notsu et al. (2024)
blueshift	60	YZ CMi	Notsu et al. (2024)
blueshift	48	YZ CMi	Notsu et al. (2024)
blueshift	70	EV Lac	Notsu et al. (2024)
blueshift	20	EV Lac	Notsu et al. (2024)
blueshift	135	AD Leo	Notsu et al. (2024)
redshift	24	V374 Peg	Vida et al. (2016)
redshift	92	M4-type star [*]	Wu et al. (2022)
redshift	300	YZ CMi	Namizaki et al. (2023)
redshift	47	AD Leo	Wollmann et al. (2023)
redshift	63	AD Leo	Wollmann et al. (2023)
redshift	90	YZ CMi	Notsu et al. (2024)
redshift	120	YZ CMi	Notsu et al. (2024)
redshift	60	YZ CMi	Notsu et al. (2024)
redshift	75	YZ CMi	Notsu et al. (2024)
redshift	90	YZ CMi	Notsu et al. (2024)
redshift	139	YZ CMi	Notsu et al. (2024)
redshift	130	YZ CMi	Notsu et al. (2024)
redshift	140	YZ CMi	Notsu et al. (2024)
redshift	50	YZ CMi	Notsu et al. (2024)
redshift	120	EV Lac	Notsu et al. (2024)
redshift	20	AD Leo	Notsu et al. (2024)

^{*} The star name was not mentioned in the paper.

Y19. Also, flare Y20 is a non-white-light flare. Almost throughout the $H\alpha$ flare, blue asymmetry is observed with the maximum velocity of $202 \pm 18 \text{ km s}^{-1}$. We found the duration of asymmetry is 160 minutes, which is the longest among $H\alpha$ blueshift events reported in publications (the longest one was 120 min in Honda et al. 2018). It is noted that the velocity was almost constant $\sim 150 \text{ km s}^{-1}$ for three hours. These characteristics are similar to the blue asymmetry event in M-dwarf EV Lac reported by Honda et al. (2018).

As discussed in 5.2.2, the typical velocities of chromospheric upflows observed in solar flares (a few 10 km s^{-1} ; Švestka et al. 1962; Tei et al. 2018; Li et al. 2019; Huang et al. 2019) are much smaller than the maximum velocity of the observed blueshifted components ($202 \pm 18 \text{ km s}^{-1}$). This suggests that chromospheric upflows are unlikely to be the cause.

Next, we discuss the possibility of prominence eruptions. The duration of the asymmetry (160 minutes) is significantly longer than those of typical prominence/filament eruptions on the Sun (several minutes to tens of minutes; e.g., Otsu et al. 2022, 2024) and those expected for M-dwarfs (\sim a few to tens of minutes). Also, the blueshifted components maintain almost constant velocity for three hours (Figure 14 (d)). If this were to be a prominence eruption, there should be some velocity changes due to the gravity. These characteristics are inconsistent with prominence eruptions.

Then, could post-flare loops be possible? In the case of the Sun, post-flare loops sometimes last more than hours (e.g., Liu et al. 2013; Song et al. 2016; Otsu et al. 2024). This is consistent with the observed long-duration asymmetry

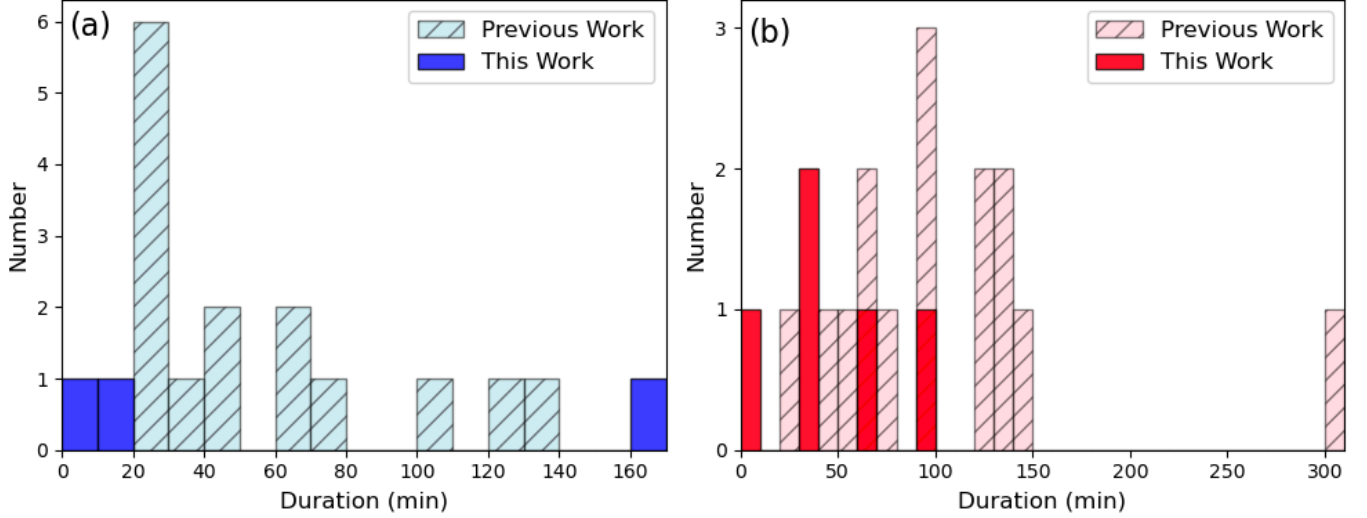


Figure 11. Comparison of the duration of asymmetry during M-dwarf flares with previous studies. (a) Comparison with previous studies on the duration of blue asymmetry. The dark blue bars represent blue asymmetry from this study, while the light blue bars represent blue asymmetry from previous studies. (b) Comparison with previous studies on the duration of red asymmetry. The dark red bars represent red asymmetry from this study, while the light red bars represent red asymmetry from previous studies.

with duration of 160 minutes. Additionally, the $H\alpha$ spectrum exhibits a blue asymmetry profile with a missing red wing (or possible redshifted absorption), suggesting the possibility of absorption by post-flare loops, similar to the red wing absorption seen in solar post-flare loops (e.g., Otsu et al. 2022, 2024). In addition, the $H\alpha$ light curve shows that gradual flares Y19 and Y20 occur following Y18. This may resemble the “peak-bump” structure observed in the TESS white-light light curve and Ca II H & K lines (Kowalski et al. 2013; Howard & MacGregor 2022). These post-flare bump features are sometimes interpreted as emissions from post-flare loops (Heinzel & Shibata 2018; Yang et al. 2023). The Sun-as-a-star analysis of post-flare loops in the $H\alpha$ line suggests that post-flare secondary peak would also be observed in the $H\alpha$ line (Otsu et al. 2024). Based on this interpretation, the Y19–20 events might represent post-flare loops emerging after the Y18 flare. However, the peak-bump structure and redshift absorption each assumes different mechanisms—emission from post-flare loops and absorption by post-flare loops, respectively—resulting in a contradiction between these interpretations. Also, Figure 9 (c) shows that the line profile exhibits a bluewing enhancement with extended velocity (or expanded “bump-like” shape centered at approximately -250 km s^{-1}). This shape cannot be solely explained by redshift absorption from the post-flare loop because the red wing absorption itself cannot make the bump-like feature in the blue wing. Therefore, all of these three hypothesis introduced in Section 5.2.1 cannot simply explain the observed properties. To fully explain the observation, we may need to consider an alternative interpretation and/or some situation specific to M-dwarfs or this event.

5.3. Origin of Rapid, Short-Duration Red Asymmetry

Flare Y6 on 2021 January 25 shows the rapid, short duration red asymmetry. Although red asymmetry is not the main focus of this paper, we discuss its origin in detail here because of its short-duration and the time variation resembling a backward prominence eruption.

Figure 5 shows the dynamic spectrum of the Y6 event and Figure 15 shows the time evolution of the equivalent width and velocity of the redshifted components. Figure 15 (a) shows that a small but significant increase in white light can be observed at the peak of the $H\alpha$ light curve in Y6. The bolometric flare energy E_{flare} is $5.80 \times 10^{30} \text{ erg}$, while the $H\alpha$ flare energy $E_{H\alpha}$ is $2.3 \times 10^{30} \text{ erg}$. It is noted that, the ratio of $H\alpha$ energy to bolometric energy is ~ 0.5 , which is relatively higher than the typical value of 0.01 to 0.1 (see Figure 18; e.g., Namekata et al. 2024). The maximum velocity of these redshifted components is $295 \pm 12 \text{ km s}^{-1}$ (Table 3). Many of previous studies have shown that the typical redshift velocity in M-dwarfs is 100–200 km s^{-1} (Vida et al. 2016; Wu et al. 2022; Wollmann et al. 2023; Notsu et al. 2024), while Namizaki et al. (2023) reported a maximum velocity of $\sim 500 \text{ km s}^{-1}$. The redshift velocity of this

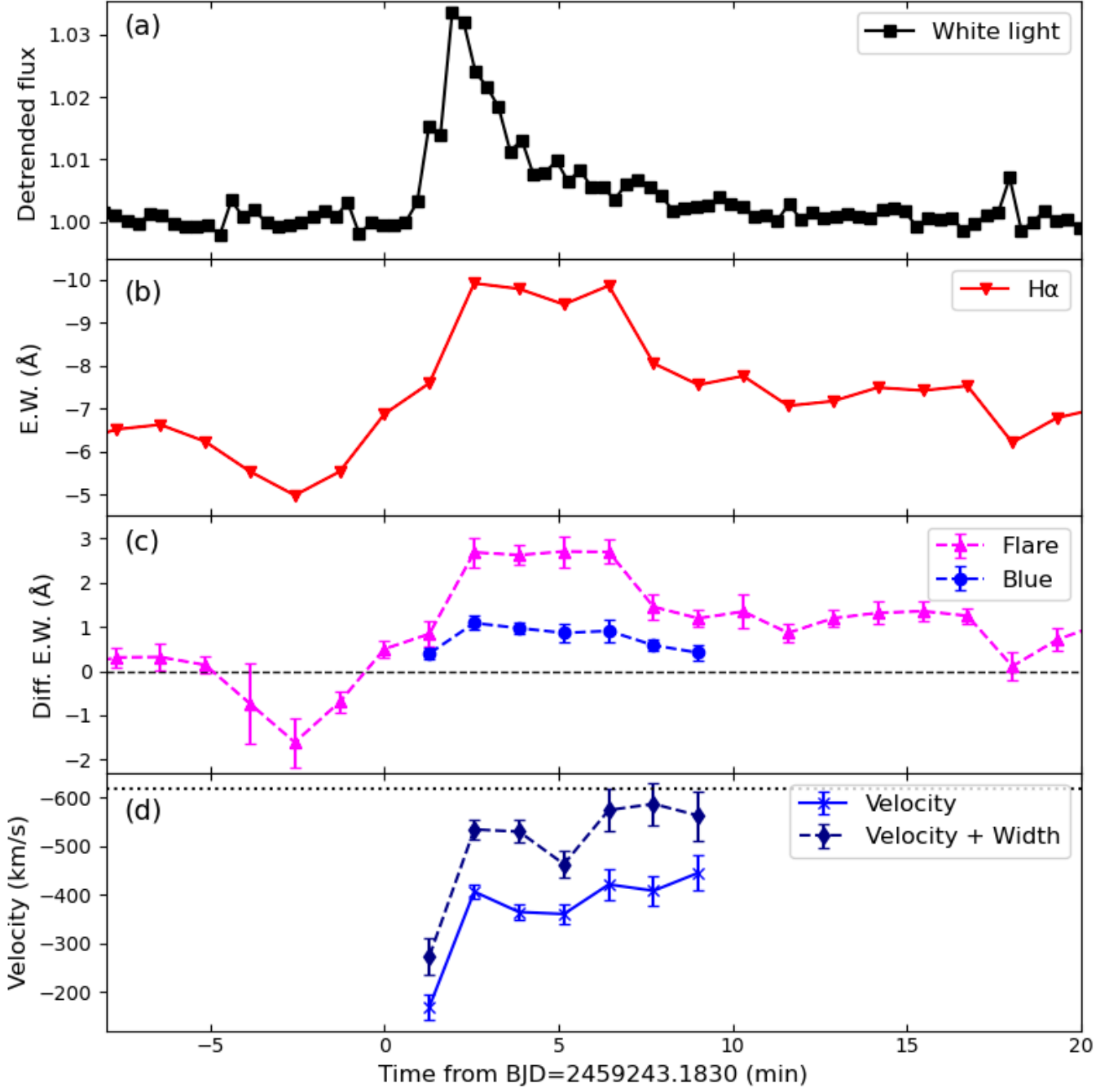


Figure 12. (a) Detrended light curve of flare Y8. The vertical axis represents the detrended flux (F/F_{star}), and the horizontal axis represents the elapsed time (in minutes) from the start of flare Y8, with BJD=2459243.1830 as the reference point. (b) Light curve of the H α line for flare Y8. The vertical axis indicates the equivalent width of H α . (c) Time evolution of the equivalent width of the flare component and the blueshifted component for flare Y8. The vertical axis shows the differential equivalent width, with magenta dashed lines indicating the variation in equivalent width of the flare component, and blue dashed lines indicating the variation in equivalent width of the blueshifted component. (d) Velocity changes of the blueshifted component of flare Y8. The vertical axis represents velocity, with a blue solid line showing the velocity changes of the blueshifted component. The navy dashed line shows the evolution of the central velocity plus the Gaussian line width σ .

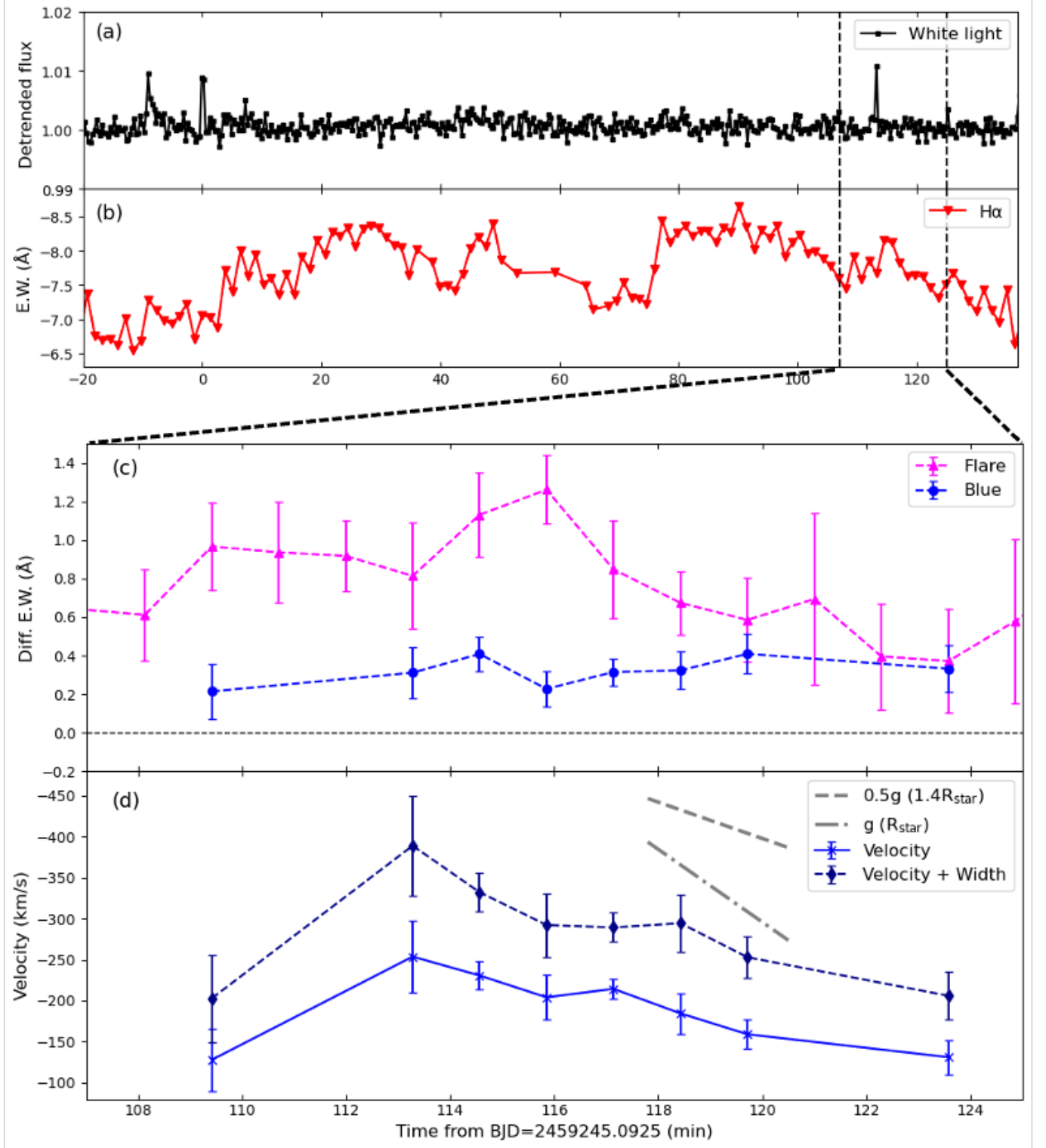


Figure 13. The same as Figure 11, but for the event of Y12. In (d), the gray dot-dashed line indicates the velocity change due to gravitational acceleration at the stellar surface, and the dashed line represents the velocity change due to 0.5 times the gravitational acceleration at the stellar surface, corresponding to the surface gravitational acceleration at $1.4R_{\text{star}}$.

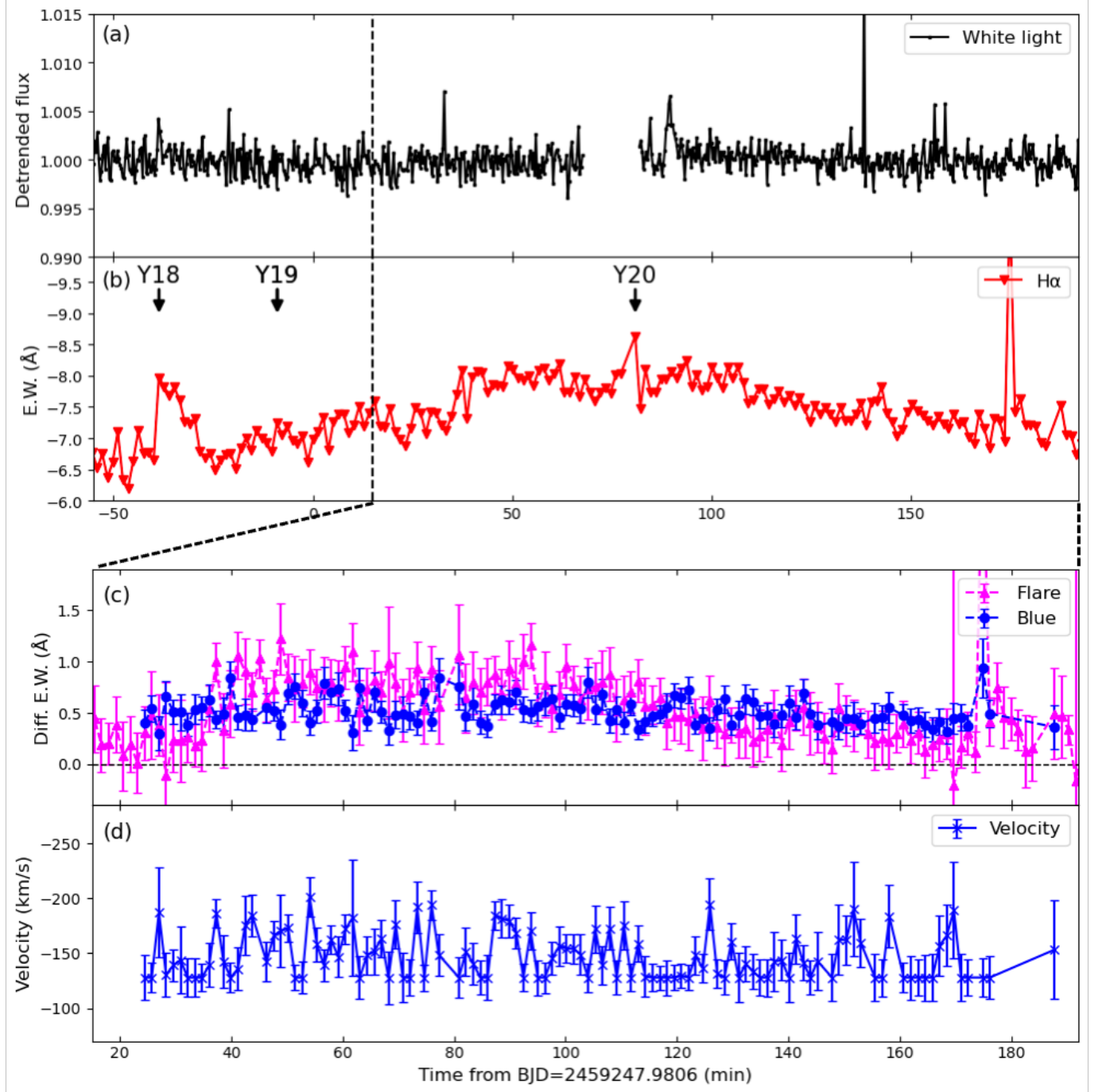


Figure 14. The same as Figure 11, but for the event of Y20. In (b), black arrows mark the peak times of flares Y18, Y19, and Y20, respectively

event is relatively faster than—but consistent with—those in these previous studies. We found that the duration of this red asymmetry is 6 minutes, which is the shortest among H α redshift events reported in publications (see Section 5.1).

The primary origins of red asymmetry in M-dwarfs are considered as chromospheric condensation and/or the downward flow of post-flare loops (e.g., Namizaki et al. 2023), but sometimes referred to backward prominence eruptions (e.g., Wu et al. 2022). In the case of the Sun, post-flare loops occur in the decay phase of a flare, and their duration often exceeds several tens of minutes. On the other hand, red asymmetry in Y6 is associated with white-light flare, an impulsive phase, at the peak of the H α . This suggests that post-flare loops are unlikely to be the cause. Next,

chromospheric condensation is thought to be formed by the compression of the chromosphere due to the high injection of high-energy non-thermal electrons (Allred et al. 2006; Longcope 2014; Kowalski et al. 2017, 2022). Therefore, a strong correlation with white-light flares originating from the chromospheric condensation region is expected (Namizaki et al. 2023). However, despite the velocity reaching $295 \pm 12 \text{ km s}^{-1}$, the accompanying white-light flare in this event is extremely faint (barely detectable). This suggests that chromospheric condensation is qualitatively unlikely to be the cause, although the possibility remains.

On the other hand, the typical velocity of solar prominence eruptions ranges from 10 to 400 km s^{-1} (Gopalswamy et al. 2003; Seki et al. 2021), and some have durations of around 5 minutes (e.g., Otsu et al. 2022). The maximum velocity of $295 \pm 12 \text{ km s}^{-1}$ and duration of approximately 6 minutes in this event are relatively fast and short but within the typical velocity and duration of solar prominence eruptions. In addition, E_{flare} ($5.8 \times 10^{30} \text{ erg}$) and $E_{\text{H}\alpha}$ ($2.3 \times 10^{30} \text{ erg}$) differ by only a factor of 2, which is strange compared to typical stellar flares. Since the TESS band includes the $\text{H}\alpha$ line, the increase in white light can be almost entirely explained by the increase in $\text{H}\alpha$ emission. This may suggest that the flare occurs around or behind the stellar limb and prominence eruption is the primary source of the $\text{H}\alpha$ radiation, which is consistent with the scenario of a backward prominence eruption.

Under the assumption that the observed redshift is a backward prominence eruption, we speculate some dynamics of the stellar eruption. Figure 15 (d) shows that the component reaches its maximum velocity already, without any acceleration phase observed. This suggests that the plasma acceleration is completed in less than 1 minute. Additionally, it decelerates over approximately 5 minutes, at a rate roughly equal to 0.5 times the surface gravitational acceleration. This may suggest the free fall of a prominence eruption that occurred at the limb and erupted at an angle of 120 degrees from the line of sight.

5.4. Implications to Stellar CMEs

In this section, we focus on the detected possible prominence eruptions and discuss their potential development into CMEs. As discussed in Section 5.2 and Section 5.3, the red/blue asymmetries observed during the three flares, Y6, Y8, and Y12, suggest prominence eruptions. The maximum velocities of these eruptions are $295 \pm 12 \text{ km s}^{-1}$, $445 \pm 36 \text{ km s}^{-1}$, and $254 \pm 43 \text{ km s}^{-1}$, respectively. Since these velocities are below the surface escape velocity of YZ CMi ($\sim 600 \text{ km s}^{-1}$), it is unclear whether the majority of prominence themselves developed into CMEs. However, in the case of the Sun, the average velocity of CMEs (610 km s^{-1}) is approximately 8 times the velocity of the associated prominence eruptions, approximately 80 km s^{-1} (Gopalswamy et al. 2003). Assuming a similar relationship between prominence eruptions and CMEs on YZ CMi, the upper layers of hot plasma associated with the prominence eruptions in Y6 & Y8, and Y12 could be accelerated to velocities of approximately 1800–3500 km/s. These velocities are much higher than the surface escape velocity of YZ CMi ($\sim 600 \text{ km s}^{-1}$). This suggests that these prominence eruptions are likely to have led to CMEs.

In addition to the central Gaussian velocity, we here mention the velocity dispersion for each event Y6, Y8, and Y20. As we described above, the observed maximum velocities of these events are below the escape velocity of YZ CMi. However, these blueshifted components are broadened more than velocity resolution $\sim 70 \text{ km s}^{-1}$ (Matsubayashi et al. 2019). In Figure 12 and Figure 13 (d), the navy diamonds indicate the evolution of the central velocity plus the Gaussian line width σ . Similarly, in Figure 15 (d), the brown diamonds show the same evolution. This can be interpreted as the velocity distribution of the expanding prominence (Namekata et al. 2024). Based on this interpretation, we can assume that the width plus central velocity can be regarded as the maximum velocity component of the eruptive prominence. In particular, we found that the velocity of Y8 almost reaches the escape velocity within the error bar, while Y6 and Y12 do not show a similar trend to Y8. This can suggest that some fast components of the eruptive prominence themselves could have developed into CMEs.

The velocity changes of the possible prominence eruptions tell us its evolution. As for the Y8, the velocity reaches its maximum at the end of the duration, with no observed deceleration afterward. This suggests that the accelerated prominence expanded spatially and became optically thin. On the other hand, although there is no velocity component faster than v_{esc} , Y6 and Y12 show no subsequent blue/red asymmetry after these red/blue asymmetries. This suggests that the prominence eruptions in Y6 and Y12 did not fall back to the stellar surface.

Next, we discuss the proportion of flares accompanied by prominence eruptions. In this research, 3 out of 27 $\text{H}\alpha$ flares ($\sim 10\%$) suggest prominence eruptions. This ratio is comparable to the value ($\sim 15\%$) reported by Notsu et al. (2024) for M-dwarfs. However, the association rate of prominence eruptions in these M-dwarfs is significantly lower compared to that in a G-dwarf ($\sim 60\%$; Namekata et al. 2024). This difference could be caused by several factors. First,

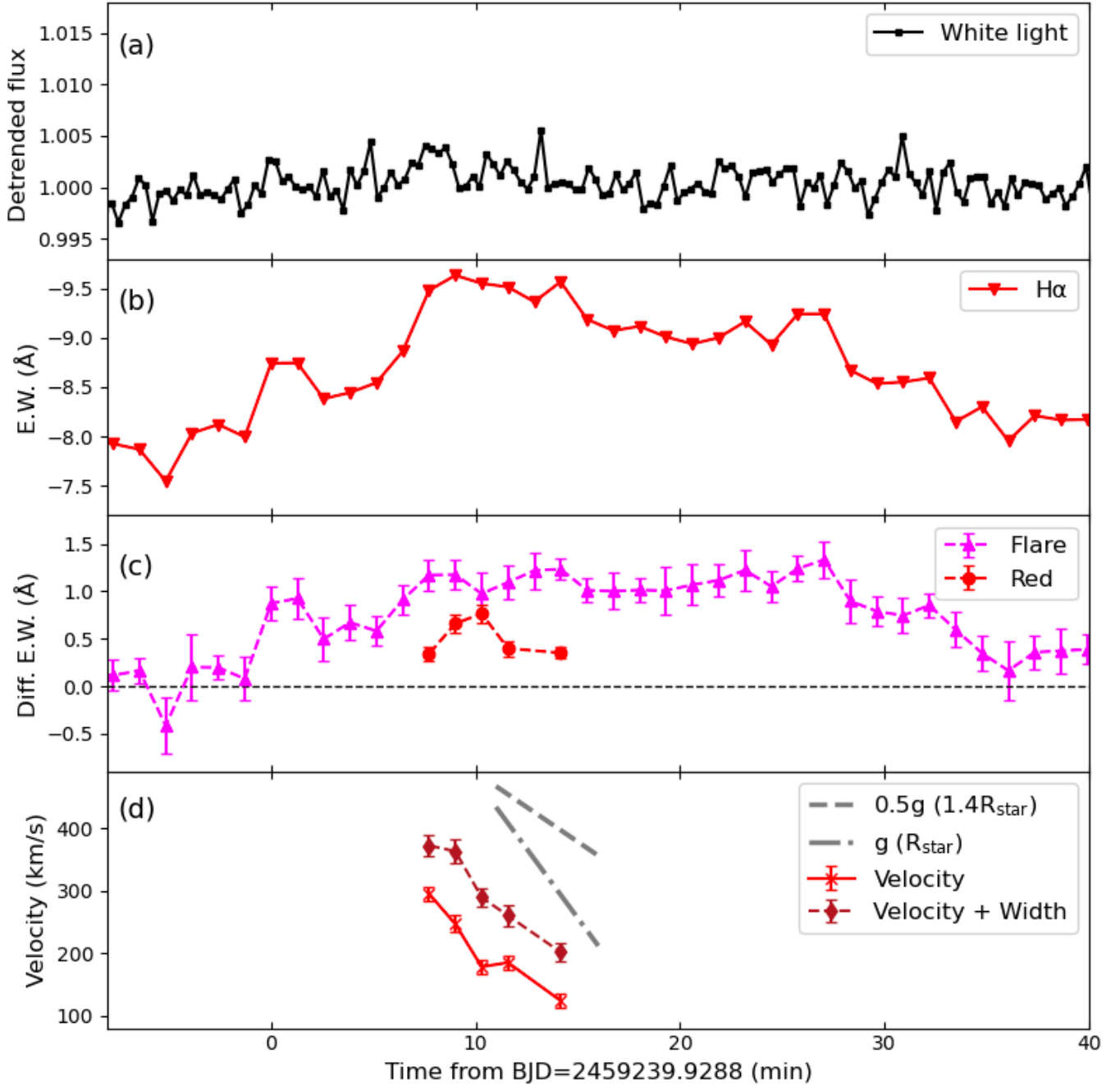


Figure 15. The same as Figure 12, but for the event of Y6. In this case, the focus is on the redshifted components.

there is a difference in the observable energy range of flares. G-dwarfs have brighter surfaces compared to M-dwarfs, making it harder to detect lower-energy flares in M-dwarfs. In the case of the Sun, higher-energy flares are more likely to be associated with eruptive events and have higher velocities (Yashiro & Gopalswamy 2009). The flares detected in G-dwarfs are relatively high-energy, potentially resulting in a higher apparent association rate of prominence eruptions compared to M-dwarfs. Second, there is a difference in the brightness contrast between the filament on the disk and the stellar surface in M-dwarfs. The surface of M-dwarfs is darker, reducing the contrast with filament on the disk, making them harder to observe (Leitzinger et al. 2022). This may have lowered the detection rate of filaments. Third, there is a difference in the coronal magnetic field strength and topology. Alvarado-Gómez et al. (2018) suggested through 3D magnetohydrodynamic simulations that CMEs could be suppressed in regions with strong overlying magnetic fields.

Fast-rotating early-mid M-dwarfs like YZ CMi have dipole-dominated or multipolar large-scale fields (Gastine et al. 2013). Zeeman Doppler Imaging observations by Morin et al. (2008); Lang et al. (2014) reported that YZ CMi had a large-scale, axisymmetric poloidal magnetic field in 2007 and 2008, with a much stronger magnetic flux than that of G-dwarfs. Therefore, the suppression of prominence eruptions due to a strong overlying magnetic field might occur more frequently in M-dwarfs.

Finally, we consider the frequency of prominence eruptions/CMEs. The total $H\alpha$ observation period was 2.8 days. During this time, we interpreted three events (Y6, Y8, Y12) as prominence eruptions. The occurrence frequency of prominence eruptions in this study is ~ 1.1 events per day, which is higher than the frequency of prominence eruptions on the Sun (0.1 to 0.4 events per day; Gopalswamy 2015) and G-dwarfs (~ 0.3 events per day; Namekata et al. 2024). As we discussed in Sections 5.2.2 and 5.3, the asymmetries in flares Y6 and Y8 which lasted less than 10 minutes, are likely caused by rapid, short-duration prominence eruptions. Since 2 out of the 3 events that we interpreted as prominence eruptions are short-duration, such events may not be rare. This suggests that previous studies of M-dwarf blue asymmetries from low time cadence spectroscopy may have underestimated the frequency of prominence eruptions/CMEs due to insufficient temporal resolution. On the other hand, the proportion of flares accompanied by prominence eruptions is comparable to the proportion reported by Notsu et al. (2024). We should note that the wavelength resolution ($R \sim 2000$) of our observation is lower than that of Notsu et al. (2024) ($R \sim 32000$). Therefore, we may have missed low-velocity prominence eruptions that Notsu et al. (2024) could detect. For future work, high time cadence (~ 1 min) and high dispersion spectroscopy are necessary to more accurately estimate the occurrence frequency of prominence eruptions/CMEs.

6. SUMMARY AND CONCLUSIONS

In this study, we conducted simultaneous photometric and spectroscopic observations of the active M-dwarf YZ CMi. As a result, we detected 27 $H\alpha$ flares and 130 white-light flares, while 17 $H\alpha$ flares are not associated with white-light flares. The $H\alpha$ flare energy $E_{H\alpha}$ ranges from 1.7×10^{29} to 3.8×10^{32} erg, and the duration ranges from 8 to 319 minutes. The bolometric energy E_{flare} ranges from 4.7×10^{30} to 1.2×10^{34} erg, and the duration ranges from 1.7 to 235.3 minutes. We introduced a new criteria based on the Bayesian Information Criterion (BIC) to identify asymmetries of $H\alpha$ line profile. Among them, 5 flares (Y4, Y5, Y6, Y16, Y21) show red asymmetries, and 3 flares (Y8, Y12, Y20) show blue asymmetries in the $H\alpha$ line profile. For red asymmetry, the maximum velocity of the redshifted components ($v_{\text{asym,max}}$) ranges from 188 to 400 km s^{-1} , with durations (τ_{asym}) ranging from 6 to 319 minutes. Similarly, for blue asymmetry, the maximum velocity of the blueshifted components ($v_{\text{asym,max}}$) also ranges from 188 to 400 km s^{-1} , with durations (τ_{asym}) ranging from 6 to 319 minutes. The physical interpretations of the red/blue asymmetries in four events (Y6, Y8, Y12, Y20) are in particular discussed in Section 5.2-5.3. The blue asymmetries are discussed in terms of chromospheric upflow, prominence eruption, and apparent blue asymmetries from the post-flare loop absorption, while red asymmetries are in terms of chromospheric condensation, post-flare loop, and backward prominence eruption. Overall, the observed relatively high blueshifted velocities (200–450 km s^{-1}) prefer the possibility of prominence eruptions for almost all cases. On the other hand, except for the observed velocity, we also found large diversities in the timing and duration of blue asymmetries and their association with the white-light flares. In particular, we discovered rapid, short-duration blue (Y8) and red (Y6) asymmetries with durations of ~ 5 minutes, thanks to an unprecedented high time-cadence (~ 1 minute) spectroscopy resolving $H\alpha$ profile. Both durations of the asymmetries are the shortest among $H\alpha$ observations reported for M-dwarfs in publications. The obtained diversities enable us to constrain their origins. We suggest that blue asymmetries from Y8 and Y12 are likely originated from prominence eruptions. Also, the red asymmetry from Y6 is likely a backward prominence eruption occurring at the limb. Y20 is the long-duration blue asymmetry lasting 160 minutes. Several aspects indicate a possibility of a post-flare loop, but there are still inconsistencies, and further study is needed. For future work, modeling studies based on observational data incorporating radiative transfer (e.g., Leitzinger et al. 2022) and further the Sun-as-a-star analysis are necessary for more detailed discussions.

The occurrence frequency of prominence eruptions is ~ 1.1 events per day. Our discovery of rapid, short-duration prominence eruptions (Y8 and Y6) indicate that previous studies with a low time cadence could have missed those events and as a result underestimate the occurrence frequency of the prominence eruptions/CMEs. Also, the low time cadence observations would miss the fast components of the prominence, which results in the underestimation of the velocity and kinetic energy of prominence eruptions (and CMEs). This relatively high velocity observed in this

study may be able to fill a gap in scaling relations for flare energy and kinetic energy between the Sun and stars (e.g., Moschou et al. 2019).

Also, in paper II, we will be focusing on the statistical viewpoints of these asymmetric events. We will investigate duration, energy, the association of white-light flares, and the rotational phase for the eruptive/non-eruptive events and discuss further what could be the source of the asymmetry.

ACKNOWLEDGMENT

We thank K. Shibata, T. Otsu, and A. Asai for their valuable comments and discussions. This research was supported by JSPS (Japan Society for the Promotion of Science) KAKENHI Grant Numbers 21J00316 (K.N.), 20K04032, 24K00685 (H.M.), and 24H00248 (Y.K., K.N., H.M., and D.N). Y.N. acknowledges the funding support from NASA ADAP 80NSSC21K0632, and NASA TESS Cycle 6 80NSSC24K0493. The spectroscopic data used in this paper were obtained through the program 21A-N-CN03 (PI: K.N.) with the 3.8m Seimei telescope, which is located at Okayama Observatory of Kyoto University. This paper includes data collected with the TESS mission, obtained from the MAST data archive at the Space Telescope Science Institute (STScI). Funding for the TESS mission is provided by the NASA Explorer Program. STScI is operated by the Association of Universities for Research in Astronomy, Inc., under NASA contract NAS 5-26555. Some of the data presented in this paper were obtained from the Mikulski Archive for Space Telescopes (MAST) at the Space Telescope Science Institute. The specific observations analyzed can be accessed via [10.17909/escv-3665](https://archive.stsci.edu/missions/tess/21A-N-CN03). The authors acknowledge ideas from the participants in the workshop “Blazing Paths to Observing Stellar and Exoplanet Particle Environments” organized by the W.M. Keck Institute for Space Studies.

Facilities: Seimei telescope, Transiting Exoplanet Survey Satellite (TESS)

Software: `astropy` (Astropy Collaboration et al. 2018), `IRAF` (Tody 1986), `PyRAF` (Science Software Branch at STScI 2012)

APPENDIX

A. APPENDIX: VELOCITY DETERMINATION ACCURACY

We fitted the normalized spectrum in the quiescent state on the day of the events showing asymmetry, using a Voigt function. From this fit, we calculated the daily mean ($\lambda_{\text{Voigt, H}\alpha}$) and the standard deviation (σ_v) of the fitted function's line center. Table 3 lists the values of $\lambda_{\text{Voigt, H}\alpha}$ and σ_v for each day. The table shows that σ_v is approximately 1-2 km s⁻¹. This value almost corresponds to the variation in the observed velocity solution during observations but is much smaller than the Gaussian fitting error used to estimate the velocity error of the asymmetric components (10-50 km s⁻¹; Table 3). Although $\lambda_{\text{Voigt, H}\alpha}$ varies within a range of 0.1 Å (~ 4.5 km s⁻¹), this value is comparable to the rotational velocity of YZ CMi ($v \sin i \sim 4.5$ km s⁻¹; [Reiners 2007](#)).

Table 5. Voigt Fit H α Line Center Measurements

Date	$\lambda_{\text{Voigt, H}\alpha}$ (Å)	σ_v (km s ⁻¹)
2021 Jan 24	6562.81	1.82
2021 Jan 25	6562.74	1.44
2021 Jan 28	6562.72	1.26
2021 Jan 30	6562.69	0.99
2021 Jan 31	6562.74	1.16
2021 Feb 02	6562.74	1.48
2021 Feb 03	6562.87	1.13

^a The mean center wavelength (Å) of the H α line determined by the Voigt fit in the quiescent state.

^b σ is the standard deviation of the fit center in the quiescent state.

B. APPENDIX: FLARE LIGHT CURVES AND DYNAMIC SPECTRUM IN THE H α LINE FOR WHICH ASYMMETRIES WERE NOT DETECTED

In this appendix, we show flare light curves and flare dynamic spectrum in H α line for which asymmetries were not detected (see Section 3.3 and Table 2). We do not discuss these events in detail, but the figures are shown in Figure 16. The figures for Y18 and Y19, which do not show asymmetries, are included in Figure 9.

Fig. Set 16. Light curves and dynamic spectrum in H α line for which asymmetries were not detected

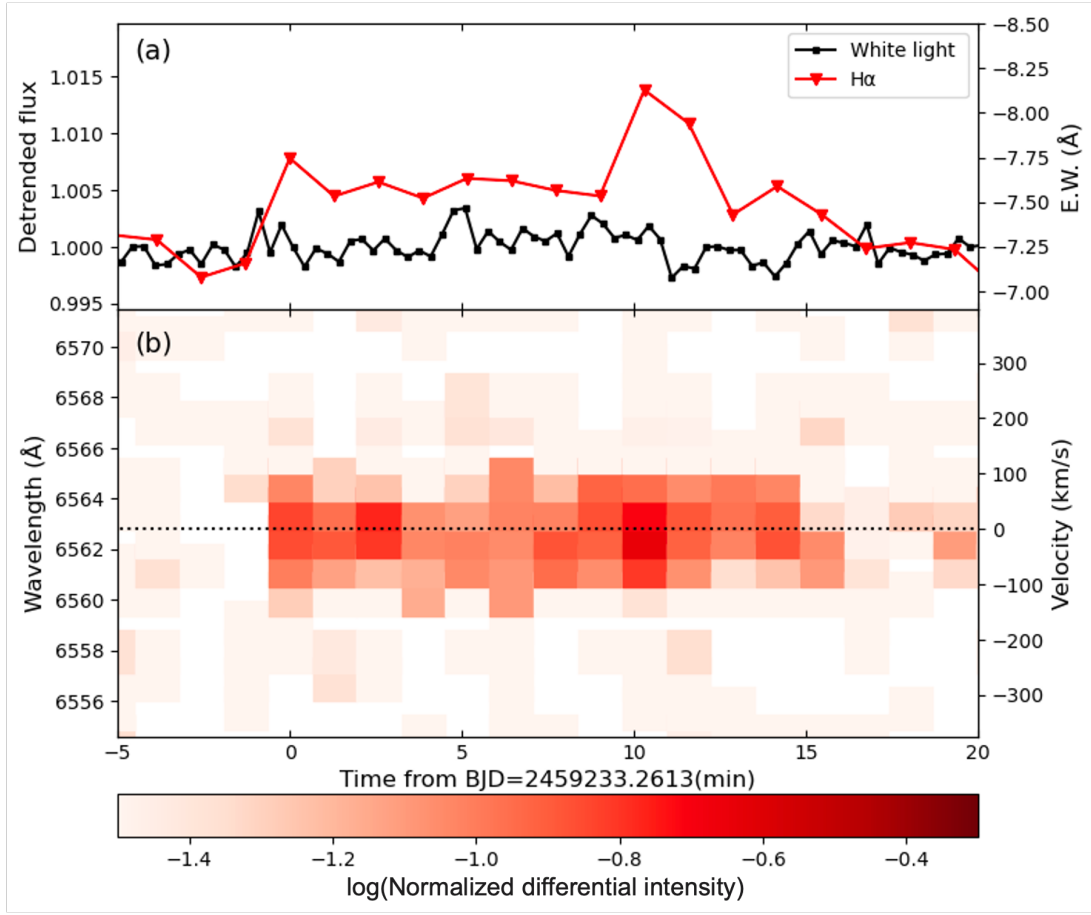


Figure 16. (a) Light curves of white light and H α line for flare Y1. The black solid line represents the detrended light curve of the white light emission showing long-term variations, and the red solid line represents the light curve of the H α line. The left vertical axis represents the detrended flux (F/F_{star}), and the right vertical axis represents the equivalent width of the H α line. (b) Temporal evolution of the H α line profile for Y1. The left vertical axis represents the wavelength, and the right vertical axis shows the Doppler velocity relative to the central wavelength of H α (6562.8Å). The horizontal axis represents the elapsed time (min) from the start of the flare, with BJD=2459233.2613 as the reference point. The color bar indicates the logarithm of the normalized intensity in the differential spectrum. Black arrows mark the time of maximum ΔBIC , and red bidirectional arrows indicate the duration of red asymmetry. (The complete figure set (15 images) is available in the online journal.)

REFERENCES

- Airapetian, V. S., Glocer, A., Gronoff, G., Hébrard, E., & Danchi, W. 2016, *Nature Geoscience* 2016 9:6, 9, 452, doi: [10.1038/ngeo2719](https://doi.org/10.1038/ngeo2719)
- Allred, J. C., Hawley, S. L., Abbett, W. P., & Carlsson, M. 2006, *ApJ*, 644, 484, doi: [10.1086/503314](https://doi.org/10.1086/503314)
- Alvarado-Gómez, J. D., Drake, J. J., Cohen, O., Moschou, S. P., & Garraffo, C. 2018, *ApJ*, 862, 93, doi: [10.3847/1538-4357/aacb7f](https://doi.org/10.3847/1538-4357/aacb7f)
- Aschwanden, M. J. 2021, arXiv e-prints, arXiv:2112.07759, doi: [10.48550/arXiv.2112.07759](https://doi.org/10.48550/arXiv.2112.07759)
- Astropy Collaboration, Price-Whelan, A. M., Sipőcz, B. M., et al. 2018, *AJ*, 156, 123, doi: [10.3847/1538-3881/aabc4f](https://doi.org/10.3847/1538-3881/aabc4f)
- Baroch, D., Morales, J. C., Ribas, I., et al. 2020, *A&A*, 641, A69, doi: [10.1051/0004-6361/202038213](https://doi.org/10.1051/0004-6361/202038213)
- Bisi, M. M., Breen, A. R., Jackson, B. V., et al. 2010, *SoPh*, 265, 49, doi: [10.1007/s11207-010-9602-8](https://doi.org/10.1007/s11207-010-9602-8)
- Švestka, Z., Kopecný, M., Blaha, M., et al. 1962, *BAICz*, 13, 37. <https://ui.adsabs.harvard.edu/abs/1962BAICz..13...37S/abstract>
- Canfield, R. C., Penn, M. J., Wulser, J.-P., & Kiplinger, A. L. 1990, *ApJ*, 363, 318, doi: [10.1086/169345](https://doi.org/10.1086/169345)
- Chang, S. W., Byun, Y. I., & Hartman, J. D. 2015, *ApJ*, 814, doi: [10.1088/0004-637X/814/1/35](https://doi.org/10.1088/0004-637X/814/1/35)
- Cifuentes, C., Caballero, J. A., Cortés-Contreras, M., et al. 2020, *A&A*, 642, A115, doi: [10.1051/0004-6361/202038295](https://doi.org/10.1051/0004-6361/202038295)
- Fabozzi, F. J., Focardi, S. M., Rachev, S. T., & Arshanapalli, B. G. 2014, Appendix E: Model Selection Criterion: AIC and BIC (Wiley), 399–403, doi: [10.1002/9781118856406.app5](https://doi.org/10.1002/9781118856406.app5)
- Fisher, G. H., Canfield, R. C., & McClymont, A. N. 1985, *ApJ*, 289, 414, doi: [10.1086/162901](https://doi.org/10.1086/162901)
- Fouqué, P., Moutou, C., Malo, L., et al. 2018, *MNRAS*, 475, 1960, doi: [10.1093/mnras/stx3246](https://doi.org/10.1093/mnras/stx3246)
- Gaia Collaboration, Vallenari, A., Brown, A. G. A., et al. 2023, *A&A*, 674, A1, doi: [10.1051/0004-6361/202243940](https://doi.org/10.1051/0004-6361/202243940)
- Gaidos, E., & Mann, A. W. 2014, *ApJ*, 791, 54, doi: [10.1088/0004-637X/791/1/54](https://doi.org/10.1088/0004-637X/791/1/54)
- Gastine, T., Morin, J., Duarte, L., et al. 2013, *A&A*, 549, L5, doi: [10.1051/0004-6361/201220317](https://doi.org/10.1051/0004-6361/201220317)
- Gilbert, E. A., Barclay, T., Schlieder, J. E., et al. 2020, *AJ*, 160, 116, doi: [10.3847/1538-3881/aba4b2](https://doi.org/10.3847/1538-3881/aba4b2)
- Gopalswamy, N. 2015, *ASSL*, 415, 381, doi: [10.1007/978-3-319-10416-4_15](https://doi.org/10.1007/978-3-319-10416-4_15)
- Gopalswamy, N. 2016, *Geoscience Letters*, 3, 8, doi: [10.1186/s40562-016-0039-2](https://doi.org/10.1186/s40562-016-0039-2)
- Gopalswamy, N., Shimojo, M., Lu, W., et al. 2003, *ApJ*, 586, 562, doi: [10.1086/367614](https://doi.org/10.1086/367614)
- Heinzel, P., & Shibata, K. 2018, *ApJ*, 859, 143, doi: [10.3847/1538-4357/aabe78](https://doi.org/10.3847/1538-4357/aabe78)
- Honda, S., Notsu, Y., Namekata, K., et al. 2018, *PASJ*, 70, 62, doi: [10.1093/PASJ/PSY055](https://doi.org/10.1093/PASJ/PSY055)
- Houdebine, E. R., Foing, B. H., & Rodono, M. 1990, *A&A*, 238, 249
- Howard, W. S., & MacGregor, M. A. 2022, *ApJ*, 926, 204, doi: [10.3847/1538-4357/ac426e](https://doi.org/10.3847/1538-4357/ac426e)
- Huang, N., Xu, Y., Sadykov, V. M., Jing, J., & Wang, H. 2019, *ApJL*, 878, L15, doi: [10.3847/2041-8213/ab2330](https://doi.org/10.3847/2041-8213/ab2330)
- Ikuta, K., Namekata, K., Notsu, Y., et al. 2023, *ApJ*, doi: [10.3847/1538-4357/acbd36](https://doi.org/10.3847/1538-4357/acbd36)
- Inoue, S., Enoto, T., Namekata, K., et al. 2024, *PASJ*, doi: [10.1093/pasj/psae001](https://doi.org/10.1093/pasj/psae001)
- Kobayashi, K., Ise, J. I., Aoki, R., et al. 2023, *Life*, 13, doi: [10.3390/life13051103](https://doi.org/10.3390/life13051103)
- Kowalski, A. F. 2024, *Living Reviews in Solar Physics*, 21, 1, doi: [10.1007/s41116-024-00039-4](https://doi.org/10.1007/s41116-024-00039-4)
- Kowalski, A. F., Allred, J. C., Carlsson, M., et al. 2022, *ApJ*, 928, 190, doi: [10.3847/1538-4357/ac5174](https://doi.org/10.3847/1538-4357/ac5174)
- Kowalski, A. F., Allred, J. C., Daw, A., Cauzzi, G., & Carlsson, M. 2017, *ApJ*, 836, 12, doi: [10.3847/1538-4357/836/1/12](https://doi.org/10.3847/1538-4357/836/1/12)
- Kowalski, A. F., Hawley, S. L., Wisniewski, J. P., et al. 2013, *ApJS*, 207, 15, doi: [10.1088/0067-0049/207/1/15](https://doi.org/10.1088/0067-0049/207/1/15)
- Kurita, M., Kino, M., Iwamuro, F., et al. 2020, *PASJ*, 72, 48, doi: [10.1093/pasj/psaa036](https://doi.org/10.1093/pasj/psaa036)
- Kurokawa, H., Hanaoka, Y., Shibata, K., & Uchida, Y. 1987, *SoPh*, 108, 251, doi: [10.1007/BF00214165](https://doi.org/10.1007/BF00214165)
- Lammer, H., Lichtenegger, H. I., Kulikov, Y. N., et al. 2007, *Astrobiology*, 7, 185, doi: [10.1089/ast.2006.0128](https://doi.org/10.1089/ast.2006.0128)
- Lang, P., Jardine, M., Morin, J., et al. 2014, *MNRAS*, 439, 2122, doi: [10.1093/mnras/stu091](https://doi.org/10.1093/mnras/stu091)
- Leitzinger, M., Odert, P., & Heinzel, P. 2022, *MNRAS*, 513, 6058, doi: [10.1093/mnras/stac1284](https://doi.org/10.1093/mnras/stac1284)
- Li, Y., Ding, M. D., Hong, J., Li, H., & Gan, W. Q. 2019, *ApJ*, 879, 30, doi: [10.3847/1538-4357/ab245a](https://doi.org/10.3847/1538-4357/ab245a)
- Lingam, M., Dong, C., Fang, X., Jakosky, B. M., & Loeb, A. 2018, *ApJ*, 853, 10, doi: [10.3847/1538-4357/aa9fef](https://doi.org/10.3847/1538-4357/aa9fef)
- Liu, K., Zhang, J., Wang, Y., & Cheng, X. 2013, *ApJ*, 768, 150, doi: [10.1088/0004-637X/768/2/150](https://doi.org/10.1088/0004-637X/768/2/150)
- Longcope, D. W. 2014, *ApJ*, 795, doi: [10.1088/0004-637X/795/1/10](https://doi.org/10.1088/0004-637X/795/1/10)
- Maehara, H., Notsu, Y., Namekata, K., et al. 2021, *PASJ*, 73, 44, doi: [10.1093/pasj/psaa098](https://doi.org/10.1093/pasj/psaa098)
- Mason, E. I., Antiochos, S. K., & Vourlidas, A. 2021, *ApJL*, 914, L8, doi: [10.3847/2041-8213/ac0259](https://doi.org/10.3847/2041-8213/ac0259)
- Matsubayashi, K., Ohta, K., Iwamuro, F., et al. 2019, *PASJ*, 71, doi: [10.1093/pasj/psz087](https://doi.org/10.1093/pasj/psz087)

- Morin, J., Donati, J. F., Petit, P., et al. 2008, *MNRAS*, 390, 567, doi: [10.1111/j.1365-2966.2008.13809.x](https://doi.org/10.1111/j.1365-2966.2008.13809.x)
- Moschou, S.-P., Drake, J. J., Cohen, O., et al. 2019, *ApJ*, 877, 105, doi: [10.3847/1538-4357/AB1B37](https://doi.org/10.3847/1538-4357/AB1B37)
- Namekata, K., Sakaue, T., Watanabe, K., et al. 2017, *ApJ*, 851, 91, doi: [10.3847/1538-4357/aa9b34](https://doi.org/10.3847/1538-4357/aa9b34)
- Namekata, K., Maehara, H., Sasaki, R., et al. 2020, *PASJ*, 72, 68, doi: [10.1093/pasj/psaa051](https://doi.org/10.1093/pasj/psaa051)
- Namekata, K., Maehara, H., Honda, S., et al. 2022, *Nature Astronomy*, 6, 241, doi: [10.1038/s41550-021-01532-8](https://doi.org/10.1038/s41550-021-01532-8)
- Namekata, K., Airapetian, V. S., Petit, P., et al. 2024, *ApJ*, 961, 23, doi: [10.3847/1538-4357/ad0b7c](https://doi.org/10.3847/1538-4357/ad0b7c)
- Namizaki, K., Namekata, K., Maehara, H., et al. 2023, *ApJ*, 945, 61, doi: [10.3847/1538-4357/acb928](https://doi.org/10.3847/1538-4357/acb928)
- Notsu, Y., Kowalski, A. F., Maehara, H., et al. 2024, *ApJ*, 961, 189, doi: [10.3847/1538-4357/AD062F](https://doi.org/10.3847/1538-4357/AD062F)
- Nutzman, P., & Charbonneau, D. 2008, *PASP*, 120, 317, doi: [10.1086/533420](https://doi.org/10.1086/533420)
- Otsu, T., Asai, A., Ichimoto, K., Ishii, T. T., & Namekata, K. 2022, *ApJ*, 939, 98, doi: [10.3847/1538-4357/ac9730](https://doi.org/10.3847/1538-4357/ac9730)
- Otsu, T., Asai, A., Ikuta, K., & Shibata, K. 2024, *ApJL*, 974, L13, doi: [10.3847/2041-8213/AD7A70](https://doi.org/10.3847/2041-8213/AD7A70)
- Reiners, A. 2007, *A&A*, 467, 259, doi: [10.1051/0004-6361:20066991](https://doi.org/10.1051/0004-6361:20066991)
- Ricker, G. R., Winn, J. N., Vanderspek, R., et al. 2015, *Journal of Astronomical Telescopes, Instruments, and Systems*, 1, 014003, doi: [10.1117/1.JATIS.1.1.014003](https://doi.org/10.1117/1.JATIS.1.1.014003)
- Science Software Branch at STScI. 2012, *Pyraf: Python alternative for IRAF*, Astrophysics Source Code Library. <http://www.ascl.net>
- Seki, D., Otsuji, K., Ishii, T. T., Asai, A., & Ichimoto, K. 2021, *Earth, Planets and Space*, 73, 58, doi: [10.1186/s40623-021-01378-4](https://doi.org/10.1186/s40623-021-01378-4)
- Shibata, K., & Magara, T. 2011, *Living Reviews in Solar Physics*, 8, 6, doi: [10.12942/LRSP-2011-6](https://doi.org/10.12942/LRSP-2011-6)
- Shibayama, T., Maehara, H., Notsu, S., et al. 2013, *ApJS*, 209, doi: [10.1088/0067-0049/209/1/5](https://doi.org/10.1088/0067-0049/209/1/5)
- Song, Q., Wang, J.-S., Feng, X., & Zhang, X. 2016, *ApJ*, 821, 83, doi: [10.3847/0004-637X/821/2/83](https://doi.org/10.3847/0004-637X/821/2/83)
- Tei, A., Sakaue, T., Okamoto, T. J., et al. 2018, *PASJ*, 70, 100, doi: [10.1093/PASJ/PSY047](https://doi.org/10.1093/PASJ/PSY047)
- Tody, D. 1986, in *Society of Photo-Optical Instrumentation Engineers (SPIE) Conference Series*, Vol. 627, *Instrumentation in astronomy VI*, ed. D. L. Crawford, 733, doi: [10.1117/12.968154](https://doi.org/10.1117/12.968154)
- van Maanen, A., van Maanen, & A. 1945, *PASP*, 57, 216, doi: [10.1086/125730](https://doi.org/10.1086/125730)
- Vida, K., Leitzinger, M., Kriskovics, L., et al. 2019, *A&A*, 623, A49, doi: [10.1051/0004-6361/201834264](https://doi.org/10.1051/0004-6361/201834264)
- Vida, K., Kriskovics, L., Oláh, K., et al. 2016, *A&A*, 590, doi: [10.1051/0004-6361/201527925](https://doi.org/10.1051/0004-6361/201527925)
- Watanabe, K., Kitagawa, J., & Masuda, S. 2017, *ApJ*, 850, 204, doi: [10.3847/1538-4357/aa9659](https://doi.org/10.3847/1538-4357/aa9659)
- Watanabe, K., Shimizu, T., Masuda, S., Ichimoto, K., & Ohno, M. 2013, *ApJ*, 776, 123, doi: [10.1088/0004-637X/776/2/123](https://doi.org/10.1088/0004-637X/776/2/123)
- Wollmann, J., Heinzel, P., & Kabáth, P. 2023, *A&A*, 669, A118, doi: [10.1051/0004-6361/202244544](https://doi.org/10.1051/0004-6361/202244544)
- Wu, Y., Chen, H., Tian, H., et al. 2022, *ApJ*, 928, 180, doi: [10.3847/1538-4357/ac5897](https://doi.org/10.3847/1538-4357/ac5897)
- Yang, K. E., Sun, X., Kerr, G. S., & Hudson, H. S. 2023, *ApJ*, 959, 54, doi: [10.3847/1538-4357/ad077d](https://doi.org/10.3847/1538-4357/ad077d)
- Yashiro, S., & Gopalswamy, N. 2009, in *IAU Symposium*, Vol. 257, *Universal Heliophysical Processes*, ed. N. Gopalswamy & D. F. Webb, 233–243, doi: [10.1017/S1743921309029342](https://doi.org/10.1017/S1743921309029342)
- Zirin, H. 1969, *SoPh*, 7, 243, doi: [10.1007/BF00224903](https://doi.org/10.1007/BF00224903)